

All-sky analysis of the general relativistic galaxy power spectrum

Jaiyul Yoo^{1,2*} and Vincent Desjacques^{3†}

¹*Institute for Theoretical Physics, University of Zürich, CH-8057 Zürich, Switzerland*

²*Lawrence Berkeley National Laboratory, University of California, Berkeley, CA 94720, U.S.A. and*

³*Département de Physique Théorique and Center for Astroparticle Physics, Université de Genève, CH-1211 Genève, Switzerland*

(Dated: February 24, 2022)

We perform an all-sky analysis of the general relativistic galaxy power spectrum using the well-developed spherical Fourier decomposition. Spherical Fourier analysis expresses the observed galaxy fluctuation in terms of the spherical harmonics and spherical Bessel functions that are angular and radial eigenfunctions of the Helmholtz equation, providing a natural orthogonal basis for all-sky analysis of the large-scale mode measurements. Accounting for all the relativistic effects in galaxy clustering, we compute the spherical power spectrum and its covariance matrix and compare it to the standard three-dimensional power spectrum to establish a connection. The spherical power spectrum recovers the three-dimensional power spectrum at each wavenumber k with its angular dependence μ_k encoded in angular multipole l , and the contributions of the line-of-sight projection to galaxy clustering such as the gravitational lensing effect can be readily accommodated in the spherical Fourier analysis. A complete list of formulas for computing the relativistic spherical galaxy power spectrum is also presented.

PACS numbers: 98.80.-k, 98.65.-r, 98.80.Jk, 98.62.Py

I. INTRODUCTION

The past few decades have seen a rapid progress in large-scale galaxy surveys. The Sloan Digital Sky Survey (SDSS; [1]) and the Two degree Field Galaxy Redshift Survey (2dFGRS; [2]) opened a new horizon in modern cosmology, mapping three-dimensional positions of millions of galaxies. The Baryonic Oscillation Spectroscopic Survey (BOSS; [3]) and the Dark Energy Survey (DES; [4]) represent the current state-of-the-art galaxy surveys, together with the recently completed WiggleZ Dark Energy Survey [5]. The exploration of the large scale structure of the Universe will continue with future galaxy surveys such as Euclid,¹ the BigBOSS,² the Large Synoptic Survey Telescope,³ and the Wide-Field InfraRed Survey Telescope.⁴ As they will cover a substantial fraction of the entire sky and a wide range of redshift, these future surveys will measure galaxy clustering with stupendous statistical power, demanding thereby that the current theoretical predictions be refined to achieve higher levels of accuracy.

The galaxy distribution measured in galaxy surveys represents a biased version of the underlying matter distribution. A traditional approach to analyzing galaxy number density fields is to utilize the power spectrum of its Fourier components. Since each Fourier mode evolves independently in the linear regime, the power spectrum measurements can be used to infer the primordial matter power spectrum and to extract cosmological information (see [6–8] for recent power spectrum measurements). While the power spectrum analysis merits its intuitively simple interpretation of the measurements in con-

nection with the underlying matter distribution, it assumes that the density fields are defined in a cubic volume. As the recent and forthcoming galaxy surveys cover a progressively larger fraction of the sky, the validity of the flat-sky approximation and the power spectrum analysis becomes questionable.

At the same time, there exists a demand for large-scale measurements from the theoretical side. In the past few years the relativistic description of galaxy clustering has been developed [9, 10]. The advance in theoretical development results from the finding that the observed quantities in galaxy clustering such as the observed redshift and the galaxy position on the sky are different from quantities used to construct the observed galaxy fluctuation such as the background redshift and the unlensed galaxy position [11]. Those theoretical quantities are gauge-dependent, and the subtle difference in those quantities become substantial on large scales, where the relativistic effect becomes important [9, 10]. The full relativistic formula of galaxy clustering can be analytically derived at the linear order in perturbations, providing a complete picture of galaxy clustering on large scales [9, 10, 12–16]. Furthermore, it is shown [17] that these relativistic effects in galaxy clustering can be measured in future galaxy surveys, providing a great opportunity to test general relativity on cosmological scales.

The relativistic formula for the observed galaxy fluctuation $\delta_g^{\text{obs}}(z, \hat{x})$ is well-defined in observations, where it is a function of the observed redshift z and angle \hat{x} on the sky. Since the wide angle formalism [18–21] has been developed to compute the two-point correlation function of the full Kaiser formula without adopting the distant-observer approximation, its extension to the full relativistic formula can be readily made [22, 23]. However, the resulting equation for the two-point correlation function is highly complicated, even for the full Kaiser formula, mainly due to the geometrical effect. Furthermore, its physical interpretation is not as straightforward as in the power spectrum analysis owing to its nontrivial relation to the primordial matter power spectrum.

Adopting the flat-sky approximation, Yoo [10] computed

*jyoo@physik.uzh.ch

†Vincent.Desjacques@unige.ch

¹ <http://sci.esa.int/euclid>

² <http://bigboss.lbl.gov>

³ <http://www.lsst.org>

⁴ <http://wfirst.gsfc.nasa.gov>

the galaxy power spectrum, accounting for the relativistic effects (see, also, [16]). While it is always possible to embed the observed sphere in a cubic volume with rectangular coordinates and to perform a power spectrum analysis, it becomes difficult in principle to connect these large-scale measurements to the underlying theory, because the flat-sky approximation has a limited range of validity. However, it is shown [24] that, on these large scales where measurement uncertainties are significant, the systematic errors associated with the flat-sky approximation are indeed negligible in the power spectrum analysis, *if performed properly*. This is consistent with the previous finding of [10, 17] obtained by a simpler treatment.

Here we present an alternative to the traditional power spectrum analysis, based on radial and angular eigenfunctions of the Helmholtz equation. The spherical Fourier analysis has been well developed [25–27] in galaxy clustering, while its application was limited to the Kaiser formula. The observed galaxy fluctuation is decomposed in terms of Fourier modes and spherical harmonics, both of which provide a natural orthogonal basis for all-sky analysis. In observational side, Fisher et al. [28] applied the spherical Fourier analysis to the IRAS Redshift Survey, and the method was further developed in Fisher et al. [26] to reconstruct the velocity and the gravitational potential fields. Theoretical refinement has been made in the past few years. Rassat and Refregier [29] computed the spherical power spectrum of the matter density with focus on the baryonic acoustic oscillation feature, ignoring the redshift-space distortion (see [30] for the effect of the redshift-space distortion and nonlinearity). Shapiro et al. [31] used the spherical Fourier analysis of the redshift-space distortion and its cross-correlation with the CMB temperature anisotropies to constrain the growth rate of structure. The same technique is also applied to the weak gravitational lensing formalism in Heavens [32] to take advantage of the information on distances to background source galaxies. Compared to the traditional weak lensing, this spherical Fourier analysis is known as the 3D weak lensing, and it is shown in Kitching et al. [33] that the 2D tomography in weak lensing is just the 3D weak lensing with the Limber approximation.

Drawing on this previous work, we perform a spherical Fourier analysis of the observed galaxy clustering. Accounting for all the general relativistic effects in galaxy clustering, we compute the spherical power spectrum and its covariance matrix and compare them to the corresponding three-dimensional power spectrum. The organization of this paper is as follows. In Sec. II, we briefly review the spherical Fourier analysis. We first discuss the basic formalism of the spherical Fourier analysis in Sec. II A and its application to galaxy redshift survey in Sec. II B. In Sec. III, we present the full general relativistic description of galaxy clustering. We first describe the key equations behind the relativistic description in Sec. III A and present its relation to the spherical Fourier analysis in Sec. III B. In Sec. III C, we provide the Limber approximation to the spherical Fourier analysis of the relativistic description. The main results of the spherical Fourier analysis are presented in Sec. IV, in which we discuss the spherical power spectrum of the relativistic formula in Sec. IV A

and the measurement uncertainties associated with them in Sec. IV B. Finally, we discuss the implications of our results in Sec. V. Our numerical calculations are performed by assuming a flat Λ CDM universe with cosmological parameters consistent with the WMAP7 results [34].

II. FORMALISM

Spherical Fourier analysis of three-dimensional density fields has been well developed [25–27] (see, also, [35] for a different approach). We briefly review the basics of spherical Fourier decomposition in Sec. II A and discuss its application to galaxy surveys in Sec. II B, accounting for issues associated with redshift distribution.

A. Spherical Fourier Decomposition

We begin by defining our normalization convention for Fourier decomposition. The position vector $|\mathbf{x}\rangle$ and the Fourier mode $|\mathbf{k}\rangle$ are normalized to satisfy the completeness relation:

$$1 = \int d^3\mathbf{x} |\mathbf{x}\rangle\langle\mathbf{x}| = \int \frac{d^3\mathbf{k}}{(2\pi)^3} |\mathbf{k}\rangle\langle\mathbf{k}|. \quad (1)$$

With the plane wave represented by

$$\langle\mathbf{x}|\mathbf{k}\rangle \equiv \exp(i\mathbf{k} \cdot \mathbf{x}), \quad (2)$$

the configuration and the Fourier space vectors are normalized as

$$\langle\mathbf{x}|\mathbf{x}'\rangle = \delta^D(\mathbf{x} - \mathbf{x}'), \quad \langle\mathbf{k}|\mathbf{k}'\rangle = (2\pi)^3 \delta^D(\mathbf{k} - \mathbf{k}'). \quad (3)$$

Given a scalar field $\delta(\mathbf{x}) \equiv \langle\mathbf{x}|\delta\rangle$, its three-dimensional Fourier components are represented as

$$\delta(\mathbf{k}) = \int d^3\mathbf{x} e^{-i\mathbf{k} \cdot \mathbf{x}} \delta(\mathbf{x}) = \int d^3\mathbf{x} \langle\mathbf{k}|\mathbf{x}\rangle\langle\mathbf{x}|\delta\rangle = \langle\mathbf{k}|\delta\rangle, \quad (4)$$

and its ensemble average defines the power spectrum as

$$\langle\delta(\mathbf{k})\delta^*(\mathbf{k}')\rangle \equiv P(\mathbf{k}, \mathbf{k}') = (2\pi)^3 \delta^D(\mathbf{k} - \mathbf{k}') P(k), \quad (5)$$

where the last equality holds if the power spectrum is rotationally and translationally invariant.

With the normalization convention, we consider a complete radial and angular basis $|klm\rangle$ in a spherical Fourier space to decompose a scalar field in three-dimensional space. We define its representation in configuration space as

$$\langle\mathbf{x}|klm\rangle \equiv \sqrt{\frac{2}{\pi}} k j_l(kr) Y_{lm}(\hat{\mathbf{x}}), \quad (6)$$

where $r = |\mathbf{x}|$, $\hat{\mathbf{x}} = (\theta, \phi)$ is a unit directional vector of \mathbf{x} , $j_l(kr)$ is a spherical Bessel function, and $Y_{lm}(\hat{\mathbf{x}})$ is a spherical

harmonics. The normalization coefficient is chosen such that the basis $|klm\rangle$ is orthonormal

$$\begin{aligned}\langle k'l'm' | klm \rangle &= \int d^3\mathbf{x} \langle k'l'm' | \mathbf{x} \rangle \langle \mathbf{x} | klm \rangle \\ &= \delta^D(k - k') \delta_{ll'} \delta_{mm'},\end{aligned}\quad (7)$$

where we used

$$\int_0^\infty dr r^2 j_l(ar) j_l(br) = \frac{\pi}{2ab} \delta^D(a - b). \quad (8)$$

By expanding the plane wave in Eq. (2)

$$\begin{aligned}\langle \mathbf{x} | \mathbf{k} \rangle &= 4\pi \sum_{lm} i^l j_l(kr) Y_{lm}^*(\hat{\mathbf{k}}) Y_{lm}(\hat{\mathbf{x}}) \\ &= (2\pi)^{3/2} \sum_{lm} \frac{i^l}{k} Y_{lm}^*(\hat{\mathbf{k}}) \langle \mathbf{x} | klm \rangle,\end{aligned}\quad (9)$$

and using the completeness condition of the $|klm\rangle$ -basis

$$\langle \mathbf{x} | \mathbf{k} \rangle = \int dk' \sum_{lm} \langle \mathbf{x} | k'lm \rangle \langle k'lm | \mathbf{k} \rangle, \quad (10)$$

we derive the relation between our spherical Fourier basis and the usual Fourier mode

$$\langle \mathbf{k} | k'lm \rangle = (2\pi)^{3/2} \frac{(-i)^l}{k} Y_{lm}(\hat{\mathbf{k}}) \delta^D(k - k'). \quad (11)$$

Naturally, the spherical Fourier basis $|klm\rangle$ encodes the amplitude $k = |\mathbf{k}|$ of the three-dimensional Fourier mode $|\mathbf{k}\rangle$ and its angular direction $Y_{lm}(\hat{\mathbf{k}})$.

Based on the $|klm\rangle$ -basis, any scalar field in configuration space can be spherically decomposed as

$$\begin{aligned}\delta(\mathbf{x}) &= \langle \mathbf{x} | \delta \rangle = \int_0^\infty dk \sum_{lm} \langle \mathbf{x} | klm \rangle \langle klm | \delta \rangle \\ &= \int_0^\infty dk \sum_{lm} \sqrt{\frac{2}{\pi}} k j_l(kr) Y_{lm}(\hat{\mathbf{x}}) \delta_{lm}(k),\end{aligned}\quad (12)$$

and its spherical Fourier mode $\delta_{lm}(k)$ is related to the three-dimensional Fourier component as

$$\delta_{lm}(k) \equiv \langle klm | \delta \rangle = \frac{i^l k}{(2\pi)^{3/2}} \int d^2\hat{\mathbf{k}} Y_{lm}^*(\hat{\mathbf{k}}) \delta(\mathbf{k}). \quad (13)$$

Due to our normalization convention of the spherical Fourier basis, the spherical Fourier mode $\delta_{lm}(k)$ is slightly different from the usual coefficient of the angular decomposition, which is just the angular integral over $\hat{\mathbf{k}}$. Finally, the spherical power spectrum $\mathcal{S}_l(k, k')$ is defined as

$$\begin{aligned}\langle \delta_{lm}(k) \delta_{l'm'}^*(k') \rangle &\equiv \delta_{ll'} \delta_{mm'} \mathcal{S}_l(k, k') \\ &= \frac{i^l (-i)^{l'} k k'}{(2\pi)^3} \int d^2\hat{\mathbf{k}} d^2\hat{\mathbf{k}}' Y_{lm}^*(\hat{\mathbf{k}}) Y_{l'm'}(\hat{\mathbf{k}}') \langle \delta(\mathbf{k}) \delta^*(\mathbf{k}') \rangle.\end{aligned}\quad (14)$$

For a rotationally and translationally invariant power spectrum in Eq. (5), the spherical power spectrum is

$$\mathcal{S}_l(k, k') = \delta^D(k - k') \mathcal{S}_l(k) = \delta^D(k - k') P(k), \quad (15)$$

and it reduces to the three-dimensional power spectrum $\mathcal{S}_l(k) = P(k)$. Equation (15) defines the three-dimensional power spectrum $\mathcal{S}_l(k)$. The three-dimensional power spectrum $\mathcal{S}_l(k)$ is independent of angular multipole l , because the underlying power spectrum is isotropic. In case of anisotropic power spectrum $P(\mathbf{k})$, $\mathcal{S}_l(k)$ will depend on angular multipole l . Using the representation $\delta(\mathbf{x})$ in configuration space, a similar but more convenient formula can be derived for the spherical Fourier mode as

$$\delta_{lm}(k) = \int d^3\mathbf{x} \sqrt{\frac{2}{\pi}} k j_l(kr) Y_{lm}^*(\hat{\mathbf{x}}) \delta(\mathbf{x}), \quad (16)$$

and its spherical power spectrum is then

$$\begin{aligned}\mathcal{S}_l(k, k') &= \frac{2kk'}{\pi} \int d^3\mathbf{x}_1 \int d^3\mathbf{x}_2 Y_{lm}^*(\hat{\mathbf{x}}_1) Y_{lm}(\hat{\mathbf{x}}_2) \\ &\quad \times j_l(kr_1) j_l(k'r_2) \langle \delta(\mathbf{x}_1) \delta(\mathbf{x}_2) \rangle.\end{aligned}\quad (17)$$

Fourier components and its power spectra are dimensionful:

$$\begin{aligned}[\delta_{lm}(k)] &= L^2, \\ [\delta(\mathbf{k})] &= [P(\mathbf{k})] = [\mathcal{S}_l(k)] = L^3, \\ [\mathcal{S}_l(k, k')] &= L^4, \quad [P(\mathbf{k}, \mathbf{k}')] = L^6.\end{aligned}\quad (18)$$

Despite the similarity to the angular power spectrum C_l analysis, the spherical Fourier power spectrum $\mathcal{S}_l(k)$ differs in a key aspect: the spherical Fourier analysis is three-dimensional, utilizing information on the radial positions of galaxies, while two-dimensional analysis like those in the CMB literature lacks the radial information. This critical difference is the advantage in the spherical Fourier analysis, where full three-dimensional Fourier modes can be mapped, whereas in two-dimensional analysis radial modes are projected along the line-of-sight direction, contributing to the power in different angular multipoles.

B. Redshift Distribution and Survey Window Function

In observation, we can only measure galaxies in the past light cone. Therefore, radial coordinates parametrized by the observed redshift carry special information, namely, *time* — quantities at two different radial coordinates are at two different redshifts. Furthermore, the mean number density $\bar{n}_g(z)$ of galaxies evolves in time, such that their fluctuation field δ_g should be properly weighted by their redshift distribution $d\bar{n}_g/dz$. This complication can be readily handled by decomposing the number density field $n_g(\mathbf{x})$, instead of its fluctuation field $\delta_g(\mathbf{x}) = n_g(\mathbf{x})/\bar{n}_g(z) - 1$, where the three-dimensional position vector \mathbf{x} is understood as a function of its radial position $r(z) = |\mathbf{x}|$ and angular position $\hat{\mathbf{x}}$.

Since the mean $\bar{n}_g(z)$ is independent of angular position,⁵

⁵ By definition, the mean $\bar{n}_g(z)$ is a quantity in a homogeneous universe, and the residual part $\delta_g(z, \hat{\mathbf{x}})$ is a fluctuation around the mean. In observation, the mean is independent of angle by construction. The two means should agree, provided that $n_g(\mathbf{x})$ is averaged over a large volume at a given redshift.

it only contributes to the monopole $\delta_{00}(k)$ in Eq. (16), and the monopole vanishes by definition at $k = 0$. Without loss of generality, we can express $\bar{n}_g(z)$ as

$$\bar{n}_g(z) \equiv \tilde{n}_g \mathcal{W}(z) \equiv \left(\frac{N_{\text{tot}}}{V_s} \right) \mathcal{W}(z), \quad (19)$$

where the surveyed volume is

$$V_s = 4\pi \int_0^\infty dr r^2 \mathcal{W} = 4\pi \int_0^\infty dz \frac{r^2}{H} \mathcal{W}, \quad (20)$$

and N_{tot} is the total number of galaxies measured in the survey. Equation (19) defines the survey window function \mathcal{W} , also known as radial selection function. It is related to the redshift distribution as

$$\mathcal{P}_z(z) = \frac{r^2}{H} \mathcal{P}_r(r) = \frac{4\pi r^2}{V_s H} \mathcal{W}(z) = \frac{4\pi r^2}{N_{\text{tot}} H} \bar{n}_g(z), \quad (21)$$

where $H(z)$ is the Hubble parameter and the normalization convention is $1 = \int dz \mathcal{P}_z(z) = \int dr r^2 \mathcal{P}_r(r)$. In principle, $\mathcal{W}(z)$ could be generalized to include an angular selection function. In what follows however, we will consider galaxy surveys with full-sky coverage and uniform angular selection function for simplicity. The galaxy number density at position \mathbf{x} thus is

$$n_g(\mathbf{x}) = \tilde{n}_g \mathcal{W}(z) [1 + \delta_g(z, \hat{\mathbf{x}})], \quad (22)$$

and its two-point correlation function reads

$$\begin{aligned} \langle n_g(\mathbf{x}_1) n_g(\mathbf{x}_2) \rangle &= \tilde{n}_g^2 \mathcal{W}(z_1) \mathcal{W}(z_2) \left[1 + \xi_g(\mathbf{x}_2 - \mathbf{x}_1) \right] \\ &\quad + \tilde{n}_g \mathcal{W}(z_1) \delta^D(\mathbf{x}_2 - \mathbf{x}_1), \end{aligned} \quad (23)$$

where $\xi_g(\mathbf{x}_2 - \mathbf{x}_1)$ is the Fourier transform of the noise-free galaxy power spectrum. We have assumed that the galaxies are an (inhomogeneous) Poisson sampling of $1 + \delta_g(\mathbf{x})$ to derive the shot-noise term [36].

Before we proceed further, we introduce the transfer functions $\mathcal{T}_X(k, z)$ of random perturbation variables X that further simplify the spherical Fourier decomposition by separating radial (time) dependence from angular dependence. For the galaxy fluctuation, we have

$$\delta_g(\mathbf{k}, z) = \mathcal{T}_g(k, z) \varphi_v(\mathbf{k}) + \epsilon(\mathbf{k}, z), \quad (24)$$

where the power spectrum of the comoving curvature $\Delta_{\varphi_v}^2(k) = k^3 P_{\varphi_v}(k)/2\pi^2$ at initial epoch is a nearly scale-invariant and the transfer function is independent of angle. The comoving curvature $\varphi_v(\mathbf{k})$ is often denoted as $\zeta(\mathbf{k})$ in literature. Arising from the discrete distribution, $\epsilon(\mathbf{k}, z)$ is a residual Poisson noise that is uncorrelated with $\delta_g(\mathbf{k}, z)$, with power spectrum $\langle \epsilon(\mathbf{k}, z) \epsilon(\mathbf{k}', z) \rangle = (2\pi)^3 \delta^D(\mathbf{k} - \mathbf{k}') / (\tilde{n}_g \mathcal{W}(z))$.

In case that time evolution is related to radial coordinates, it is more natural to use Eq. (16) than Eq. (13), and so is it to use Eq. (17) than Eq. (14) for computing spherical Fourier modes and their spherical power spectrum, respectively. On inserting Eq. (22) into Eq. (16) and substituting the transfer function \mathcal{T}_g

and survey selection function \mathcal{W} , the spherical Fourier mode simplifies to

$$\begin{aligned} \delta_{lm}(k) &= i^l \int \frac{d \ln k' k'^3}{2\pi^2} \int d^2 \hat{\mathbf{k}}' \varphi_v(\mathbf{k}') Y_{lm}^*(\hat{\mathbf{k}}') \mathcal{M}_l(k', k) \\ &\quad + \epsilon_{lm}(k), \end{aligned} \quad (25)$$

where $\epsilon_{lm}(k)$ is the spherical Fourier transform of the residual noise field $\tilde{n}_g \mathcal{W}(z) \epsilon(\mathbf{x})$, and the spherical multipole function $\mathcal{M}_l(k', k)$ is defined as

$$\mathcal{M}_l(\tilde{k}, k) \equiv k \sqrt{\frac{2}{\pi}} \int_0^\infty dr r^2 \mathcal{W}(r) j_l(\tilde{k}r) j_l(kr) \mathcal{T}_g(\tilde{k}, r), \quad (26)$$

where its dimension is $[\mathcal{M}_l(\tilde{k}, k)] = L^2$. After some simplification, the spherical power spectrum in Eq. (17) eventually reads

$$\begin{aligned} S_l(k, k') &= 4\pi \tilde{n}_g^2 \int d \ln \tilde{k} \Delta_{\varphi_v}^2(\tilde{k}) \mathcal{M}_l(\tilde{k}, k) \mathcal{M}_l(\tilde{k}, k') \\ &\quad + \frac{2kk'}{\pi} \tilde{n}_g \int_0^\infty dr r^2 \mathcal{W}(r) j_l(kr) j_l(k'r). \end{aligned} \quad (27)$$

The second-term in the right-hand side is the shot-noise contribution. Using the Limber approximation (see Sec. III C), the shot-noise power spectrum can be rewritten as

$$\begin{aligned} \mathcal{N}_l(k, k') &\equiv \frac{2kk'}{\pi} \tilde{n}_g \int_0^\infty dr r^2 \mathcal{W}(r) j_l(kr) j_l(k'r) \\ &\approx \tilde{n}_g \mathcal{W}(\nu/k) \delta^D(k - k'), \end{aligned} \quad (28)$$

where $\nu = l + 1/2$. For a homogeneous and isotropic galaxy population with constant comoving number density $\bar{n}_g = \tilde{n}_g$ and power spectrum $\langle \delta_g(\mathbf{k}) \delta_g^*(\mathbf{k}') \rangle = (2\pi)^3 \delta^D(\mathbf{k} - \mathbf{k}') P_g(k)$, the spherical power spectrum Eq. (27) yields the well-known relation

$$S_l(k) = \bar{n}_g^2 P_g(k) + \bar{n}_g. \quad (29)$$

The angular multipole l controls the transverse wavenumber k_\perp but, since the amplitude of the wavevector $k = |\mathbf{k}|$ is already set in $S_l(k)$, the spherical power spectrum must be independent of l . In practice, however, $\mathcal{W}(r)$ is always different than unity so that $S_l(k, k)$ is never independent of the multipole l . Note also that, with the galaxy number density defined as Eq. (22), both the spherical power spectra S_l and \mathcal{N}_l have dimensions of L^{-2} . We will henceforth assume that V_s is accurately known and work with the normalized galaxy number density $n_g(\mathbf{x})/\tilde{n}_g$, instead of $n_g(\mathbf{x})$. In this case, the spherical power spectrum is given by the right-hand side of Eq. (27) divided by \tilde{n}_g^2 .

Before we close this section and apply the spherical Fourier analysis to the general relativistic description of galaxy clustering, we discuss our assumption for survey geometry and other approaches to handling the survey window function. Our spherical Fourier decomposition assumes that the full sky is available for measuring the galaxy number density field $n_g(\mathbf{x})$. For surveys with an incomplete sky coverage, angular multipoles with characteristic scale larger than the sky

coverage are simply unavailable, while angular multipoles on smaller scales remain unaffected.

In literature, the radial boundary condition is often imposed by choosing discrete wavenumbers k_{n_l} , in which the range of integer n_l depends on angular multipole l (e.g., [26, 27, 31]). Since the galaxy number density can be measured only within the survey region, the number density field outside the survey volume is set zero in those approaches. Hence, this situation is equivalent to solving the Poisson equation within the survey area and the Laplace equation outside the survey [26]. A unique solution can be singled out on imposing Dirichlet or Neumann conditions at the boundary (or a linear combination thereof) [27]. Therefore, despite the same number density measured within the survey region, the resulting potential and velocity fields are different due to the non-locality of their relation to the density field, depending on the choice of boundary conditions. As we are interested in describing the observed galaxy number density $n_g^{\text{obs}}(\mathbf{x})$, rather than the other derived quantities such as velocity or potential, no boundary condition need be imposed, and the results for $n_g^{\text{obs}}(\mathbf{x})$ are identical in all approaches, whenever our continuous wavenumbers equal discrete ones or the survey volume becomes infinite.

III. GALAXY CLUSTERING IN GENERAL RELATIVITY

Here we present the full relativistic description of galaxy clustering in Sec. III A. Weight functions are derived to facilitate the full calculations of the spherical galaxy power spectrum in Sec. III B and simplified Limber formulas are presented in Sec. III C to provide physical insight.

A. General Relativistic Description of Galaxy Clustering

Since the standard approach to modeling galaxy clustering is based on the Newtonian framework, it naturally breaks down on large scales, where relativistic effect becomes significant. Recently, the fully relativistic description of galaxy clustering was formulated [9, 10], resolving gauge issues between observable and unobservable quantities. The key finding in the theoretical development is that unobservable quantities such as the true redshift and the unlensed galaxy position are gauge-dependent. Therefore, we need to construct galaxy clustering statistics based on observables quantities like the galaxy redshift and the position on the sky. In doing so, effects such as redshift-space distortions and lensing magnification are naturally incorporated. Hence, this approach provides a unified description of various effects in galaxy clustering [11].

The relativistic description of galaxy clustering can be derived from the fact that the number dN_g^{obs} of observed galaxies in a small volume is conserved:

$$dN_g^{\text{obs}} = n_g^{\text{obs}} dV_{\text{obs}} = n_g^{\text{phy}} dV_{\text{phy}}, \quad (30)$$

and this equation defines the observed galaxy number density

n_g^{obs} with the observed volume element

$$dV_{\text{obs}}(z) = \frac{r^2(z)}{H(z)} \sin \theta \, dz \, d\theta \, d\phi, \quad (31)$$

described by the observed galaxy position (θ, ϕ) on the sky and the observed redshift z . The “observed” volume element dV_{obs} is different from the “physical” volume dV_{phy} occupied by the observed galaxies on the sky, and the distortion between these two volume elements, so called the volume effect, gives rise to contributions to the observed galaxy fluctuation. While the dominant contribution in the volume effect is the redshift-space distortion and the gravitational lensing effect, there exist other subtle relativistic contributions, and the physical volume can be obtained by tracing the photon path backward (see [9, 10] for details in deriving dV_{phy} and computing the volume effect).

Another source of fluctuations in galaxy clustering is the source effect describing the distortion associated with the physical galaxy number density n_g^{phy} . The mean galaxy number density is obtained by averaging the observed galaxy number density at the observed redshift, which differs from the proper time at the galaxy rest frame. The contribution of this source effect is proportional to the evolution bias factor of the galaxy number density

$$e = 3 + \frac{d \ln \bar{n}_g}{d \ln(1+z)}, \quad (32)$$

where the factor three in Eq. (32) appears because we use the comoving number density \bar{n}_g . Other contributions of the source effect can arise, depending on how we define the galaxy sample at hand (see [9–11, 17]). In typical galaxy surveys, galaxy samples are defined with the observed luminosity inferred from the observed flux, which is different from the intrinsic luminosity. So the source effect associated with it is then proportional to the luminosity function slope

$$p = -0.4 \frac{d \log \bar{n}_g}{d \log L}, \quad (33)$$

where the luminosity L is computed by using the observed flux and the observed redshift.

Putting all these effects together and accounting for the relativistic contributions, the general relativistic description of the observed galaxy fluctuation can be written, to the linear order in perturbation, as [9, 10]

$$\begin{aligned} \delta_g^{\text{obs}} = & b \delta_v - e \delta z_v - 5p \delta \mathcal{D}_L + \alpha_\chi + 2 \varphi_\chi + V \\ & + 3 \delta z_\chi - H \frac{d}{dz} \left(\frac{\delta z_\chi}{\mathcal{H}} \right) + 2 \frac{\delta \mathcal{R}}{r} - 2 \mathcal{K}, \end{aligned} \quad (34)$$

where the linear bias factor is b , the comoving gauge matter density is δ_v , the lapse term δz in the observed redshift is defined as $1+z = (1+\bar{z})(1+\delta z)$, the dimensionless fluctuation in the luminosity distance is $\delta \mathcal{D}_L$, the gauge-invariant temporal and spatial metric perturbations are α_χ and φ_χ , the line-of-sight velocity is V , and the gauge-invariant radial displacement and lensing convergence are $\delta \mathcal{R}$ and \mathcal{K} . The subscripts χ and v represent that the gauge-invariant quantities

with the corresponding subscript are identical to those quantities evaluated in the conformal Newtonian gauge ($\chi = 0$) or in the dark matter comoving gauge ($v = 0$), in which the shear seen by the normal observer vanishes ($\chi = 0$) or the off-diagonal component of the energy momentum tensor vanishes ($v = 0$), respectively. Note that α_χ and φ_χ correspond to the Bardeen's variables Φ_A and Φ_H [37] and we have assumed no vector and tensor contributions in Eq. (34). We refer the reader to [9, 10, 17] for details in the derivation (see also [12–16]).

Equation (34) is written in a physically transparent way. The observed galaxy fluctuation is modulated by the matter density δ_v , and there exist additional contributions from the source and the volume effects. The source effect is composed of $e \delta z_v$ and $5p \delta \mathcal{D}_L$, and the other terms in Eq. (34) come from the volume effect. Of the volume effect, the last three terms in the first line of Eq. (34) defines the rest frame of the observed galaxies, and the remaining terms in the second line describe the distortion of the comoving volume element in Eq. (31). It is noted that the term $3 \delta z_\chi$ accounts for the distortion in the comoving volume factor a^3 and in Eq. (31) the conversion between the comoving and the physical volume elements is based on the observed redshift.

In order to compute the observed galaxy fluctuation δ_g^{obs} , we need to evaluate the individual gauge-invariant variables in Eq. (34). While Eq. (34) is arranged in terms of gauge-invariant variables to explicitly ensure the gauge-invariance of δ_g^{obs} , it can be computed with any choice of gauge conditions, but preferably with the most convenient for computation. Using the Einstein equations, we have the following relation for a flat Λ CDM universe [37–41],

$$\phi \equiv \varphi_\chi = -\alpha_\chi = \frac{3H_0^2}{2} \frac{\Omega_m}{ak^2} \delta_m, \quad (35)$$

$$v \equiv v_\chi = -\frac{1}{k} \delta'_m = -\frac{\mathcal{H}f}{k} \delta_m, \quad (36)$$

where the comoving gauge matter density is obtained upon setting $\delta_m \equiv \delta_v$. and the logarithmic growth rate is $f = d \ln \delta_m / d \ln a$. Other gauge-invariant variables in Eq. (34) can

be readily expressed in terms of δ_m , v , and ϕ as [17]

$$V = \frac{\partial}{\partial r} \int \frac{d^3 \mathbf{k}}{(2\pi)^3} \frac{-v}{k} e^{i\mathbf{k} \cdot \mathbf{x}}, \quad (37)$$

$$\delta z_\chi = V + \phi + \int_0^r d\tilde{r} \, 2\phi', \quad (38)$$

$$\delta z_v = \delta z_\chi + \int \frac{d^3 \mathbf{k}}{(2\pi)^3} \frac{\mathcal{H}v}{k} e^{i\mathbf{k} \cdot \mathbf{x}}, \quad (39)$$

$$\delta \mathcal{R} = -\frac{\delta z_\chi}{\mathcal{H}} - \int_0^r d\tilde{r} \, 2\phi, \quad (40)$$

$$\mathcal{K} = -\int_0^r d\tilde{r} \left(\frac{r - \tilde{r}}{\tilde{r}r} \right) \hat{\nabla}^2 \phi, \quad (41)$$

$$\delta \mathcal{D}_L = \frac{\delta \mathcal{R}}{r} + \delta z_\chi + \phi - \mathcal{K}, \quad (42)$$

$$-H \frac{d}{dz} \left(\frac{\delta z_\chi}{\mathcal{H}} \right) = -V - \frac{1+z}{H} \phi' - \frac{1+z}{H} \frac{\partial V}{\partial r} - \delta z_\chi + \frac{1+z}{H} \frac{dH}{dz} \delta z_\chi. \quad (43)$$

We also note that the total derivative in Eq. (43) is along the past light cone: $dr = dz/H$ and $dr = \partial r - \partial \tau$.

B. Fourier Decomposition and Weight Function

Now that all the contributions in Eq. (34) can be expressed in terms of the matter density δ_m and its transfer function $\mathcal{T}_m(k, r)$, we define the weight functions $W_i(\mathbf{x}, \mathbf{k})$ for each contribution in Eq. (34) through the following decomposition of the observed galaxy fluctuation:

$$\delta_g^{\text{obs}}(\mathbf{x}) = \sum_i \int_0^r d\tilde{r} \int \frac{d^3 \mathbf{k}}{(2\pi)^3} W_i(\tilde{\mathbf{x}}, \mathbf{k}) \mathcal{T}_m(k, \tilde{r}) \varphi_v(\mathbf{k}) e^{i\mathbf{k} \cdot \tilde{\mathbf{x}}} + \epsilon(\mathbf{x}), \quad (44)$$

where the observed galaxy position is $\mathbf{x} = [r(z), \hat{\mathbf{x}}]$ and the line-of-sight position is $\tilde{\mathbf{x}} = (\tilde{r}, \hat{\mathbf{x}})$ in spherical coordinates ($\mathbf{x}/\|\mathbf{x}\|$). The dimension of the weight functions is $[W_i(\tilde{\mathbf{x}}, \mathbf{k})] = L^{-1}$, and $\epsilon(\mathbf{x})$ is the residual shot-noise field.

Categorically, each contribution in Eq. (34) can be classified in three different types according to its dependence on the angle $\hat{\mathbf{x}}$ and the line-of-sight distance \tilde{r} . The first and simplest type includes all the contributions such as δ_v , α_χ , and φ_χ that are independent of $\hat{\mathbf{x}}$ and \tilde{r} . For example, the matter density in Eq. (34) is

$$\delta_v(\mathbf{x}) = \delta_m(\mathbf{x}) = \int \frac{d^3 \mathbf{k}}{(2\pi)^3} \mathcal{T}_m(k, r) \varphi_v(\mathbf{k}) e^{i\mathbf{k} \cdot \mathbf{x}}, \quad (45)$$

and hence the weight function for the matter density takes the simplest form

$$W(\tilde{\mathbf{x}}, \mathbf{k}) = \delta^D(r - \tilde{r}). \quad (46)$$

Similarly, the weight function for the potential $\varphi_\chi = \phi$ is

$$W(\tilde{\mathbf{x}}, \mathbf{k}) = \delta^D(r - \tilde{r}) \frac{3H_0^2}{2} \frac{\Omega_m}{ak^2}. \quad (47)$$

TABLE I: Weight functions of the observed galaxy fluctuation in Eq. (44). All the perturbation variables in Eq. (34) are scaled with the matter density in the dark-matter comoving gauge by using the Einstein equations, and its relations to the matter density are defined as the weight functions that can be used for computing the spherical multipole function in Eq. (54) and the spherical power spectrum in Eq. (57). Time dependent quantities a , H , and f are evaluated at the observed redshift z , and those with tilde depend on the line-of-sight distance \tilde{r} (or the corresponding redshift $\tilde{z} \leq z$).

gauge-invariant quantity	weight function $W_l(r, \tilde{r}, k)$
δ_v	$\delta^D(r - \tilde{r})$
α_χ	$-\delta^D(r - \tilde{r}) \frac{3H_0^2}{2} \frac{\Omega_m}{ak^2}$
φ_χ	$\delta^D(r - \tilde{r}) \frac{3H_0^2}{2} \frac{\Omega_m}{ak^2}$
V	$\delta^D(r - \tilde{r}) \left(\frac{\mathcal{H}f}{k} \frac{\partial}{k\partial r} \right)$
δz_χ	$\delta^D(r - \tilde{r}) \left[\left(\frac{\mathcal{H}f}{k} \frac{\partial}{k\partial r} \right) + \frac{3H_0^2}{2} \frac{\Omega_m}{ak^2} \right] + 3H_0^2 \Omega_m \frac{\tilde{H}(\tilde{f}-1)}{k^2}$
δz_v	$\delta^D(r - \tilde{r}) \left[\left(\frac{\mathcal{H}f}{k} \frac{\partial}{k\partial r} \right) + \frac{3H_0^2}{2} \frac{\Omega_m}{ak^2} - \frac{\mathcal{H}^2 f}{k^2} \right] + 3H_0^2 \Omega_m \frac{\tilde{H}(\tilde{f}-1)}{k^2}$
$\frac{\delta \mathcal{R}}{r}$	$-\delta^D(r - \tilde{r}) \left[\left(\frac{\mathcal{H}f}{k} \frac{\partial}{k\partial r} \right) + \frac{3H_0^2}{2} \frac{\Omega_m}{ak^2} \right] - \frac{3H_0^2}{\mathcal{H}r} \Omega_m \frac{\tilde{H}(\tilde{f}-1)}{k^2} - \frac{3H_0^2}{r} \frac{\Omega_m}{\tilde{a}k^2}$
$-H \frac{d}{dz} \left(\frac{\delta z_\chi}{\mathcal{H}} \right)$	$-\delta^D(r - \tilde{r}) \left[\left(2 - \frac{1+z}{H} \frac{dH}{dz} \right) \left(\frac{\mathcal{H}f}{k} \frac{\partial}{k\partial r} \right) + \frac{3H_0^2}{2} \frac{\Omega_m}{ak^2} \left(f - \frac{1+z}{H} \frac{dH}{dz} \right) + f \frac{\partial^2}{(k\partial r)^2} \right] - 3H_0^2 \Omega_m \left(1 - \frac{1+z}{H} \frac{dH}{dz} \right) \frac{\tilde{H}(\tilde{f}-1)}{k^2}$
\mathcal{K}	$\frac{3H_0^2}{2} \Omega_m l(l+1) \left(\frac{r-\tilde{r}}{\tilde{r}r} \right) \frac{1}{\tilde{a}k^2}$
$\delta \mathcal{D}_L$	$\delta^D(r - \tilde{r}) \left[\left(1 - \frac{1}{\mathcal{H}r} \right) \left(\frac{\mathcal{H}f}{k} \frac{\partial}{k\partial r} \right) + \frac{3H_0^2}{2} \frac{\Omega_m}{ak^2} \left(2 - \frac{1}{\mathcal{H}r} \right) \right] + \frac{3H_0^2}{k^2} \Omega_m \left[\tilde{H}(\tilde{f}-1) \left(1 - \frac{1}{\mathcal{H}r} \right) - \frac{1}{\tilde{a}r} - \frac{l(l+1)}{2\tilde{a}} \left(\frac{r-\tilde{r}}{\tilde{r}r} \right) \right]$

Fluctuations of the second type depend on the observed angle, yet are independent of the line-of-sight distance. This applies to the line-of-sight velocity contribution V (and functions thereof such as δz_χ , $\delta \mathcal{R}$, $\delta \mathcal{D}_L$),

$$\begin{aligned} V(\mathbf{x}) &= \frac{\partial}{\partial r} \int \frac{d^3 \mathbf{k}}{(2\pi)^3} \left(\mathcal{H} f \frac{\delta_m}{k^2} \right) e^{i\mathbf{k} \cdot \mathbf{x}} \\ &= \int \frac{d^3 \mathbf{k}}{(2\pi)^3} \frac{\mathcal{H} f}{k} \mathcal{T}_m(k, r) \varphi_v(\mathbf{k}) \left(\frac{\partial}{k\partial r} \right) e^{i\mathbf{k} \cdot \mathbf{x}}, \end{aligned} \quad (48)$$

of which the weight function is

$$W(\tilde{\mathbf{x}}, \mathbf{k}) = \delta^D(r - \tilde{r}) \left(\frac{\mathcal{H} f}{k} \frac{\partial}{k\partial r} \right). \quad (49)$$

The derivative operator acts on the radial component of the plane wave in Eq. (44).

Finally, the third type covers the contributions along the line-of-sight direction that are independent of the observed angle. This category includes numerous line-of-sight integrals in Eqs. (38)–(42), including the Sachs-Wolfe effect and the weak lensing convergence. For example, the Sachs-Wolfe contribution in δz_χ in Eq. (38) can be decomposed as

$$\begin{aligned} \int_0^r d\tilde{r} \phi' &= \int_0^r d\tilde{r} \int \frac{d^3 \mathbf{k}}{(2\pi)^3} \phi(\mathbf{k}, \tilde{r})' e^{i\mathbf{k} \cdot \tilde{\mathbf{x}}} \\ &= \int_0^r d\tilde{r} \int \frac{d^3 \mathbf{k}}{(2\pi)^3} \left[\frac{3H_0^2}{2} \Omega_m \frac{\tilde{H}(\tilde{f}-1)}{k^2} \right] \mathcal{T}_m(k, \tilde{r}) \varphi_v(\mathbf{k}) e^{i\mathbf{k} \cdot \tilde{\mathbf{x}}}, \end{aligned} \quad (50)$$

and, therefore, the resulting weight function is

$$W(\tilde{\mathbf{x}}, \mathbf{k}) = \frac{3H_0^2}{2} \Omega_m \frac{\tilde{H}(\tilde{f}-1)}{k^2}, \quad (51)$$

where \tilde{H} and \tilde{f} depend on \tilde{r} and we used $\phi' = \mathcal{H}\phi(f-1)$. Another example of this type is the weak lensing convergence

in Eq. (41)

$$\begin{aligned} \mathcal{K} &= - \int_0^r d\tilde{r} \left(\frac{r - \tilde{r}}{\tilde{r}r} \right) \hat{\nabla}^2 \int \frac{d^3 \mathbf{k}}{(2\pi)^3} \phi(\mathbf{k}, \tilde{r}) e^{i\mathbf{k} \cdot \tilde{\mathbf{x}}} \\ &= - \int_0^r d\tilde{r} \int \frac{d^3 \mathbf{k}}{(2\pi)^3} \left[\left(\frac{r - \tilde{r}}{\tilde{r}r} \right) \frac{3H_0^2}{2\tilde{a}k^2} \Omega_m \right] \\ &\quad \times \mathcal{T}_m(k, \tilde{r}) \varphi_v(\mathbf{k}) \hat{\nabla}^2 e^{i\mathbf{k} \cdot \tilde{\mathbf{x}}}. \end{aligned} \quad (52)$$

The weight functions depend on position r , wavevector k , and line-of-sight distance \tilde{r} , and its angular dependence can be removed by using the plane wave expansion, i.e.,

$$W_l(r, \tilde{r}, k) = \frac{3H_0^2}{2} \Omega_m l(l+1) \left(\frac{r - \tilde{r}}{\tilde{r}r} \right) \frac{1}{\tilde{a}k^2}, \quad (53)$$

where the expansion factor \tilde{a} depends on \tilde{r} and the angular part of the plane wave satisfies $\hat{\nabla}^2 Y_{lm}(\tilde{\mathbf{x}}) = -l(l+1)Y_{lm}(\tilde{\mathbf{x}})$. For convenience, Table I summarizes all the weight functions.

With the full Fourier decomposition of the observed galaxy fluctuation, the spherical multipole function in Eq. (26) must be generalized as follows to take into proper account each component in Eq. (44),

$$\begin{aligned} \mathcal{M}_l^i(\tilde{k}, k) &\equiv k \sqrt{\frac{2}{\pi}} \int_0^\infty dr r^2 \mathcal{W}(r) j_l(kr) \\ &\quad \times \int_0^r d\tilde{r} W_l^i(r, \tilde{r}, \tilde{k}) \mathcal{T}_m(\tilde{k}, \tilde{r}) j_l(\tilde{k}\tilde{r}), \end{aligned} \quad (54)$$

and the spherical multipole function of the observed galaxy fluctuation is simply

$$\mathcal{M}_l(\tilde{k}, k) = \sum_i \mathcal{M}_l^i(\tilde{k}, k). \quad (55)$$

The spherical power spectrum of the observed (normalized) galaxy fluctuation is then

$$\mathcal{S}_l(k, k') \equiv \bar{\mathcal{S}}_l(k, k') + \mathcal{N}_l(k, k'), \quad (56)$$

where $\bar{\mathcal{S}}_l(k, k')$ is the noise-free galaxy power spectrum,

$$\bar{\mathcal{S}}_l(k, k') = 4\pi \int d \ln \tilde{k} \Delta_{\varphi_v}^2(\tilde{k}) \mathcal{M}_l(\tilde{k}, k) \mathcal{M}_l(\tilde{k}, k'), \quad (57)$$

and the noise component is

$$\mathcal{N}_l(k, k') \equiv \frac{2kk'}{\pi \tilde{n}_g} \int_0^\infty dr r^2 \mathcal{W}(r) j_l(kr) j_l(k'r), \quad (58)$$

where \mathcal{S}_l is identical to Eq. (27) except for a factor of \tilde{n}_g^2 . Its dimension thus is L^4 .

The weight functions defined here differ from those in [9], as we scale all the perturbation variables with the matter density in the comoving gauge. This approach is better suited to numerical computation, but its applicability is limited to a flat universe with a pressureless component, including a cosmological constant and baryons on large scales. For different cosmological models or modified gravity theories, the relation among δ_v , α_χ , φ_χ , and v_χ is in general different [42–44] from what we assumed for a pressureless medium, and one should use the weight functions in [9] with the corresponding transfer functions.

C. Limber Approximation

Before we present numerical calculations of the spherical power spectrum in Sec. IV, we adopt the Limber approximation to derive analytic formulas for the spherical multipole functions and the spherical power spectra. The Limber approximation ([45–47]) relies on the fact that the spherical Bessel function $j_l(x)$ peaks at $x \approx \nu \equiv l + 1/2$ and oscillates rapidly for $x \gtrsim \nu$. For large values of angular multipole l , integrals of product of a smooth function $f(x)$ times $j_l(x)$ can be approximated by

$$\int_0^\infty dx f(x) j_l(x) \simeq \sqrt{\frac{2}{\pi \nu}} f(\nu) [1 + \mathcal{O}(1/\nu^2)]. \quad (59)$$

With aid of the orthogonality relation for the spherical Bessel functions, this result can also be written as [48]

$$\begin{aligned} \frac{\pi}{2} \int_0^\infty dr r^2 f(r) j_l(kr) j_l(k'r) &\simeq \frac{\delta^D(k - k')}{k^2} \\ &\times f(\nu/k) [1 + \mathcal{O}(1/\nu^2)]. \end{aligned} \quad (60)$$

In the case of the matter density, for instance, we obtain the spherical multipole function

$$\mathcal{M}_l^\delta(\tilde{k}, k) \approx \sqrt{\frac{\pi}{2k^2}} \mathcal{W}(\nu/k) \mathcal{T}_m\left(k, \frac{\nu}{k}\right) \delta^D(k - \tilde{k}), \quad (61)$$

and the spherical power spectrum

$$\mathcal{S}_l^\delta(k, k') \approx \mathcal{W}(\nu/k)^2 P_m\left(k, \frac{\nu}{k}\right) \delta^D(k - k'). \quad (62)$$

Similarly, on using the Limber approximation, the spherical power spectrum $\mathcal{S}_l^\phi(k, k')$ of the potential perturbation can

be readily computed owing to the simple dependence of the spherical multipole function on the weight function. The noise contribution to the spherical power spectrum falls in the same category, and the Limber approximation gives

$$\mathcal{N}_l(k, k') \approx \frac{1}{\tilde{n}_g} \mathcal{W}(\nu/k) \delta^D(k - k'). \quad (63)$$

In addition, the Limber approximation can greatly simplify the computation of the projected quantities such as the Sachs-Wolfe contribution and the gravitational lensing contribution. These quantities contain two line-of-sight integrations in the spherical multipole function in Eq. (54), each of which involves the spherical Bessel function. With the Limber approximation, the spherical multipole function of the gravitational lensing is

$$\begin{aligned} \mathcal{M}_l^\mathcal{K}(\tilde{k}, k) &\simeq \sqrt{\frac{\pi}{2\tilde{k}^2}} \mathcal{W}(\nu/k) \frac{3H_0^2}{2} \Omega_m \mathcal{T}_m(\tilde{k}, \nu/\tilde{k}) \\ &\times l(l+1) \left(\frac{\tilde{k} - k}{\tilde{a} k^2 \tilde{k}^2} \right), \end{aligned} \quad (64)$$

where \tilde{a} is the expansion factor at $\tilde{r} = \nu/\tilde{k}$. The spherical power spectrum $\mathcal{S}_l^\mathcal{K}(k, k')$ of the gravitational lensing is then obtained by integrating the spherical multipole function over \tilde{k} , instead of a quintuple integration over \tilde{k} and two pairs (r, \tilde{r}) .

The spherical multipole function of the line-of-sight velocity or the redshift-space distortion involves the derivatives of the spherical Bessel function, since their weight function acts on the radial component as in Eq. (48). Since derivatives of the spherical Bessel function $j_l(x)$ are linear combinations of spherical Bessel functions at different angular multipoles, they do not form an orthogonal basis. In these cases, we find that the Limber approximation becomes less accurate, and next-leading corrections are required to enhance the accuracy. Despite this shortcoming in a few cases, the Limber approximation provides nonetheless a simple and physical explanation of the complicated spherical power spectrum. Therefore, we will frequently rely on it when we discuss the physical interpretation of the full numerical results in Sec. IV.

IV. OBSERVED SPHERICAL POWER SPECTRUM

Here we present the observed spherical power spectrum in Sec. IV A and compare to the corresponding flat-sky three-dimensional power spectrum. The measurement uncertainties associated with the spherical power spectrum are presented in Sec. IV B.

A. Spherical Power Spectrum

For definiteness we consider all-sky galaxy surveys with two different survey window functions. Figure 1 plots two survey window functions $\mathcal{W}(r)$ and their corresponding redshift distribution $\mathcal{P}_z(z)$. We consider two specific window

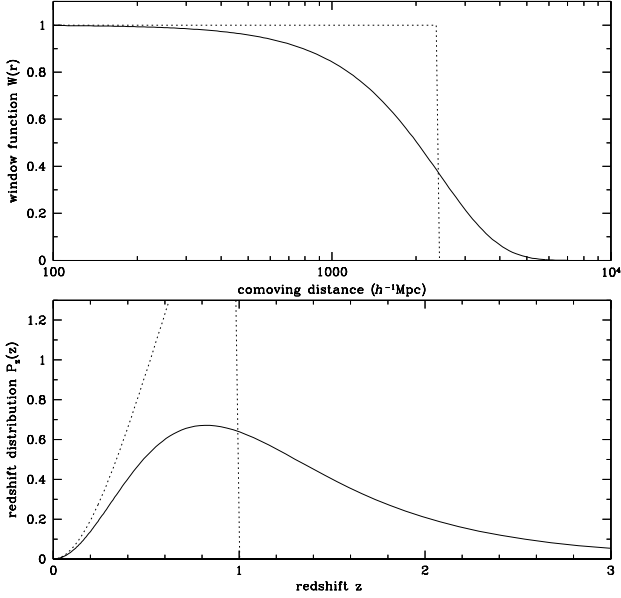


FIG. 1: Survey window functions \mathcal{W} and redshift distributions P_z . Upper panel: Gaussian window function (solid) in Eq. (65) and top-hat window function (dotted) in Eq. (66). Bottom panel: Corresponding redshift distributions obtained by using Eq. (21). The characteristic scales r_0 of the surveys are set equal to the comoving distance to $z = 1$. The comoving number density is related to the survey window function as in Eq. (19).

functions that approximately represent a flux-limited survey (solid) and a volume-limited survey (dotted), if the comoving number density $\bar{n}_g(z)$ is constant. Survey window functions (top panel) are related to galaxy redshift distributions (bottom panel) via Eqs. (19) and (21), and hence to the evolution bias factor in Eq. (32). The former window function is modeled as a Gaussian (solid)

$$\mathcal{W}(r) = \exp \left[- \left(\frac{r}{r_0} \right)^2 \right], \quad (65)$$

and the latter window function is modeled as a top-hat (dotted)

$$\mathcal{W}(r) = \begin{cases} 1, & r \leq r_0, \\ 0, & r > r_0, \end{cases} \quad (66)$$

where the characteristic distance or the survey depth is $r_0 = 2354 h^{-1} \text{Mpc}$ set equal to the comoving distance to $z = 1$. In both cases, the redshift distribution rises with redshift as more volume becomes available, but it drops sharply at r_0 for the volume-limited survey, while the tail of the flux-limited survey extends to higher redshift $z \geq 1$. By defining the spherical Fourier modes through Eq. (16), we are implicitly assuming that the galaxy overdensity $\delta_g(\mathbf{x})$ is pixelized. Therefore, the survey window function $\mathcal{W}(r)$ should in principle include a pixel window function. For simplicity, however, we will ignore this complication and assume that the data has been deconvolved.

Figure 2 illustrates the spherical power spectra of representative components of the full general relativistic formula δ_g^{obs} in Eq. (34), such as the matter density δ_m , the line-of-sight velocity V , the gravitational potential ϕ , and so on (see Eqs. [37]–[43]). The Gaussian window function is adopted in computing the spherical power spectra. For simplicity, we first assume that the matter transfer function $\mathcal{T}_m(k, z)$ is independent of redshift (i.e., of the line-of-sight distance \tilde{r}) and the redshift-dependent quantities in the weight functions $W_l^i(r, \tilde{r}, k)$ such as a , H , and f are set equal to those evaluated at $z = 0$ when computing the spherical multipole functions $\mathcal{M}_l^i(\tilde{k}, k)$ in Eq. (54). The spherical multipole function is then integrated over \tilde{k} to obtain the spherical power spectrum $\mathcal{S}_l(k)$ by using Eq. (57). The full spherical galaxy power spectrum $\mathcal{S}_l^{\text{obs}}(k)$ is the sum of the auto and the cross power spectra of all the components in Eq. (34), which can be readily deduced from Fig. 2 (see also [10]).

The first column shows the spherical power spectra $\mathcal{S}_l(k)$ of the matter density δ_m (solid) and the redshift-space distortion $\frac{1+z}{H} \frac{\partial V}{\partial r}$ (dashed) as a function of wavenumber k and angular multipole l . Each row shows the same spherical power spectra but at different angular multipoles, ranging from $l = 2$ (top) to $l = 10$ (bottom). Since the matter density power spectrum $P_m(k)$ is isotropic, the spherical power spectrum $\mathcal{S}_l^{\delta}(k)$ (solid) of the matter density is independent of angular multipole, and it reduces to the three-dimensional power spectrum $P_m(k) \simeq \mathcal{S}_l^{\delta}(k)$ (gray solid). Given angular multipole l in each row, the characteristic wavenumber $k_c \equiv l/r_0$ is shown as the vertical lines, below which the power is highly suppressed and well beyond which the equality of two power spectra holds. Technically, the power is suppressed at $k \ll k_c$ due to the spherical Bessel function $j_l(kr) \simeq 0$ at $kr \ll l$, and the physical interpretation is that larger scale modes $k \ll k_c \simeq k_{\perp}$ cannot be measured given the survey depth r_0 . The match between $\mathcal{S}_l^{\delta}(k)$ and $P_m(k)$ could be extended to larger scales, if more survey volume is available than what is assumed here.

For the Gaussian survey window function we adopted here, there exists an analytic formula for the spherical multipole function $\mathcal{M}_l^{\delta}(k', k)$. Using Eq. (6.633) in Gradshteyn and Ryzhik [49] and setting $\lambda = 0$ and $\mu = \nu = l$, a useful identity can be derived as

$$\int_0^{\infty} dx x^2 e^{-\alpha x^2} j_l(\beta x) j_l(\gamma x) = \frac{\pi e^{-\frac{\beta^2 + \gamma^2}{4\alpha}}}{4\alpha \sqrt{\beta\gamma}} I_{l+\frac{1}{2}} \left(\frac{\beta\gamma}{2\alpha} \right), \quad (67)$$

where the modified Bessel function is $I_{\nu}(z) = (-i)^{\nu} J_{\nu}(iz)$. If we again ignore the time evolution of the transfer function $\mathcal{T}_m(k, z) \simeq \mathcal{T}_m(k)$, the spherical multipole function of the matter density is [29]

$$\mathcal{M}_l^{\delta}(k', k) = \sqrt{\frac{\pi}{2k'^2}} \mathcal{T}_m(k') \frac{r_0^2 \sqrt{kk'}}{2} e^{-\frac{(k^2 + k'^2)r_0^2}{4}} I_{l+\frac{1}{2}} \left(\frac{r_0^2 kk'}{2} \right), \quad (68)$$

and in the limit $r_0^2 kk' \gg 2l(l+1)$ (valid at small scales) it reduces to

$$\mathcal{M}_l^{\delta}(k', k) = \sqrt{\frac{\pi}{2k'^2}} \mathcal{T}_m(k') \times \left[\frac{r_0}{\sqrt{4\pi}} e^{-\frac{(k-k')^2}{4} r_0^2} \right], \quad (69)$$

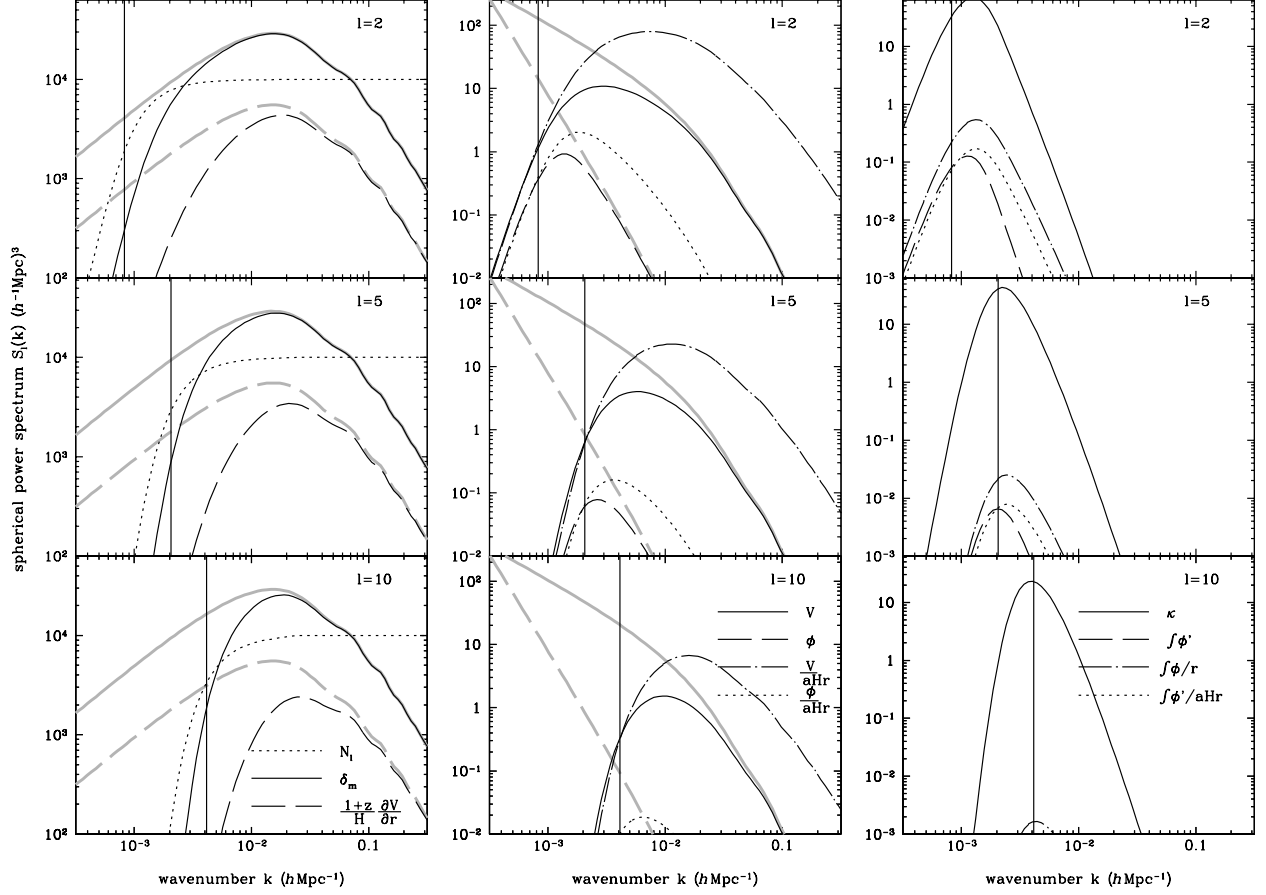


FIG. 2: Spherical power spectra with Gaussian window function. In each panel, various curves with labels show the spherical power spectra of representative components of the full general relativistic formula δ_g^{obs} in Eq. (34), which are further decomposed in Eqs. (37)–(43). The time evolution of the transfer and the weight functions is ignored, and their values are set equal to those at $z = 0$. Each column plots the same spherical power spectra at angular multipoles, ranging from $l = 2$ (top rows) to $l = 10$ (bottom rows), illustrating their angular dependence. Vertical lines mark the characteristic wavenumber $k_c \equiv l/r_0$, below which spherical power spectra are suppressed due to the constraint $k \geq k_\perp \simeq k_c$. Gray curves show the three-dimensional power spectra at $z = 0$, if there exist well-defined correspondences. For example, spherical power spectra for the density (solid) and the redshift-space distortion (dashed) in the first column reduce to the corresponding three-dimensional power spectra on small scales. The noise power spectrum (dotted) is shown in the first column, assuming $\tilde{n}_g = 10^{-4} (h^{-1} \text{Mpc})^{-3}$. Compared to the contributions in the first two columns, the projected quantities in the third column are negligible, except the gravitational lensing convergence. The turn-over of the spherical power spectra on large scales reflects the limit set by survey depth \sim a few times $1/r_0$. These large-scale modes can be recovered by deconvolving the survey window function.

where the Gaussian wavepacket in the square bracket converges towards the Dirac distribution in the limit of infinite volume ($r_0 \rightarrow \infty$). The resulting spherical multipole function is independent of angular multipole l , reflecting the fact that high- k modes do not feel the r -dependence of the Gaussian window function.

At sufficiently high k , where $\mathcal{M}_l^\delta(k', k)$ is well described by Eq. (69), the spherical power spectrum in Eq. (57) becomes

$$\begin{aligned} \mathcal{S}_l^\delta(k, k) &\simeq \int d\tilde{k} P_m(\tilde{k}) \left[\frac{r_0}{\sqrt{4\pi}} e^{-\frac{(k-\tilde{k})^2}{4} r_0^2} \right]^2 \\ &\simeq P_m(k) \frac{r_0}{2\sqrt{2\pi}}, \end{aligned} \quad (70)$$

and we define the three-dimensional spherical power spectrum

as

$$\mathcal{S}_l^\delta(k) = \mathcal{S}_l^\delta(k, k) \left(\frac{r_0}{2\sqrt{2\pi}} \right)^{-1}. \quad (71)$$

Equation (70) reduces to Eq. (15), if the volume is infinite. Since numerical integrations of the spherical power spectrum in Eq. (57) require fine sampling and prone to numerical errors due to the highly oscillating nature of the spherical Bessel functions in $\mathcal{M}_l(k, k)$, we tested our numerical calculations against the analytic solution, and both results agree to high precision.

Next, the dashed curves in the first column represent the redshift-space distortion contribution $\frac{1+z}{H} \frac{\partial V}{\partial r}$. Since there is only one line-of-sight direction in the plane parallel limit,

the redshift-distortion contribution is conveniently expressed in terms of cosine angle $\mu_k = \hat{\mathbf{x}} \cdot \hat{\mathbf{k}}$ between the line-of-sight $\hat{\mathbf{x}}$ and the wavevector \mathbf{k} , and its three-dimensional power spectrum is $P_z(k, \mu_k) = f^2 \mu_k^4 P_m(k)$. Thin dashed curves show the spherical power spectrum $S_l^z(k)$ of the redshift-space distortion, while the gray dashed curves in each row show $P_z(k, \mu_k = 1) = f^2 P_m(k)$ for comparison. As the angular multipole becomes higher at a given $k = |\mathbf{k}|$, more angular modes are emphasized (or equivalently lower μ_k), and the spherical power spectrum $S_l^z(k)$ decreases. At $k \gg k_c$, the spherical power spectrum reduces to the three-dimensional power spectrum $P_z(k, \mu_k)$ with its angular dependence encoded in angular multipole in each row.

The second column plots the spherical power spectra of the dominant relativistic corrections to the observed galaxy fluctuation δ_g^{obs} , such as the line-of-sight velocity V (solid), the gravitational potential ϕ (dashed), and their linear combinations in Eqs. (37)–(43). Since the velocity and the potential contributions scale as (k/\mathcal{H}) and $(k/\mathcal{H})^2$ relative to the matter density δ_m , these relativistic contributions are comparable only at the horizon scale $k \simeq \mathcal{H}$ and constitute small corrections in most galaxy surveys (see [17] for measuring these effects).

The spherical power spectrum $S_l^\phi(k)$ (dashed) of the gravitational potential ϕ follows the three dimensional power spectrum $P_\phi(k)$ (gray dashed) at each row, whose amplitude quickly decreases at high k as $P_\phi(k) \propto k^{-3}$, but is independent of angular multipole l . At a given small k , the amplitude $S_l^\phi(k)$ becomes lower in the lower panels, simply because $k \leq k_c$ (the vertical line in each row again illustrates the characteristic minimum wavenumber k_c given angular multipole l). The angular dependence of the line-of-sight velocity V means that its spherical power spectrum $S_l^V(k)$ (solid) also depends on angular multipole l and it decreases with increasing angular multipole (or smaller μ_k) on all scales, in addition to the effect at $k \leq k_c$. Since the three dimensional power spectrum of the line-of-sight velocity is $P_V(k, \mu_k) = \mu_k^2 P_v(k) = (\mathcal{H}f/k)^2 \mu_k^2 P_m(k)$, we plot $P_V(k, \mu_k = 1)$ (gray solid) at each row for comparison, and again the spherical power spectrum $S_l^V(k)$ reduces to the three-dimensional power spectrum $P_V(k, \mu_k)$. Last, the dotted curves show the noise power spectrum $\mathcal{N}_i(k)$ for a galaxy sample with $\bar{n}_g = 10^{-4} (h^{-1} \text{Mpc})^{-3}$. For the Gaussian radial selection function, the shot-noise contribution to $S_l(k, k')$ can be computed exactly by using Eq. (67) as

$$\mathcal{N}_i(k, k') = \frac{1}{2} \frac{r_0^2}{\bar{n}_g} \sqrt{k k'} e^{-\frac{r_0^2}{4}(k^2 + k'^2)} I_{l+\frac{1}{2}} \left(\frac{r_0^2 k k'}{2} \right), \quad (72)$$

and it asymptotically matches the Poisson power spectrum $1/\bar{n}_g$ on small scales.

The remaining two curves show the variants of the line-of-sight velocity and the gravitational potential, $V/\mathcal{H}r$ (dot dashed) and $\phi/\mathcal{H}r$ (dotted). They both arise due to the radial distortion $\delta\mathcal{R}/r$. With the prefactor $1/\mathcal{H}r$ in those terms, more weight is given to shorter distance r , and hence they peak at a slightly higher wavenumber k than their counterparts without the prefactor, while the shift in the peak position depends on the adopted window function.

The last column shows the spherical power spectra of the projected quantities along the line-of-sight direction, such as the gravitational lensing \mathcal{K} (solid), the integrated Sachs-Wolfe effect $\int_0^r d\tilde{r} \phi'$ (dashed), the Sachs-Wolfe effect $\int_0^r d\tilde{r} \phi/\tilde{r}$ (dot-dashed), and their linear combinations in Eqs. (37)–(43). Since these contributions are intrinsically angular and their variations are largely limited to the transverse direction, the angular power spectrum C_l is often used to characterize them, and there is no exact analogy to the usual three-dimensional power spectrum for the projected quantities (see, however, [50]). Apart from the gravitational lensing convergence, the spherical power spectra of the projected quantities are at least an order-of-magnitude smaller than the gravitational potential ϕ in the second column. Those projected quantities are isotropic and independent of angular multipole, with the sole exception of the gravitational lensing \mathcal{K} , whose additional angular dependence $l(l+1)$ arises due to the angular Laplacian operator. The spherical power spectrum of the gravitational lensing \mathcal{K} exactly corresponds to the 3D weak lensing [32, 33, 51], where the same spherical Fourier analysis is applied to background source galaxies to map the foreground matter distribution. While two more shear fields are available in weak lensing measurements, only the convergence field \mathcal{K} contributes to galaxy clustering.

In Fig. 3, we show the spherical power spectra with the top-hat window function in Eq. (66) and discuss its effect on the spherical power spectra, compared to those in Fig. 2. We have again ignored the time evolution of the transfer and the weight functions for simplicity. Three-dimensional power spectra shown as gray curves in Fig. 3 are identical to those in Fig. 2. The normalization of the spherical power spectra can be obtained in a similar manner by considering the spherical power spectrum of the matter density,

$$S_l^\delta(k, k) = \int d\tilde{k} P_m(\tilde{k}) \left[\frac{2 k \tilde{k}}{\pi} \int_0^{r_0} dr r^2 j_l(kr) j_l(\tilde{k}r) \right]^2, \quad (73)$$

and taking the limit $k \rightarrow \infty$ (see Appendix A)

$$\lim_{k \rightarrow \infty} S_l^\delta(k, k) = P_m(k) \frac{r_0}{\pi} \sqrt{\frac{3}{\pi}}. \quad (74)$$

Therefore, we plot the spherical power spectra in Fig. 3 as

$$S_l(k) = S_l(k, k) \left(\frac{r_0}{\pi} \sqrt{\frac{3}{\pi}} \right)^{-1}. \quad (75)$$

The spherical power spectra of the matter density (solid) and the redshift-space distortion (dashed) in the first column are nearly identical to their counterparts with the Gaussian window function. The prominent difference is the oscillations in $S_l(k)$ at $k \leq 2\pi/(r_0/3)$, where most contributions to $S_l(k)$ at those low k arise near $r \simeq r_0$ and the highly oscillating spherical Bessel function is abruptly truncated at the survey boundary $r = r_0$, causing incomplete cancellation of the oscillations. The noise power spectrum (dotted) is nearly constant under the top-hat survey window function. With full weight given $\mathcal{W}(r) = 1$ near $r \leq r_0$, however, the recovery

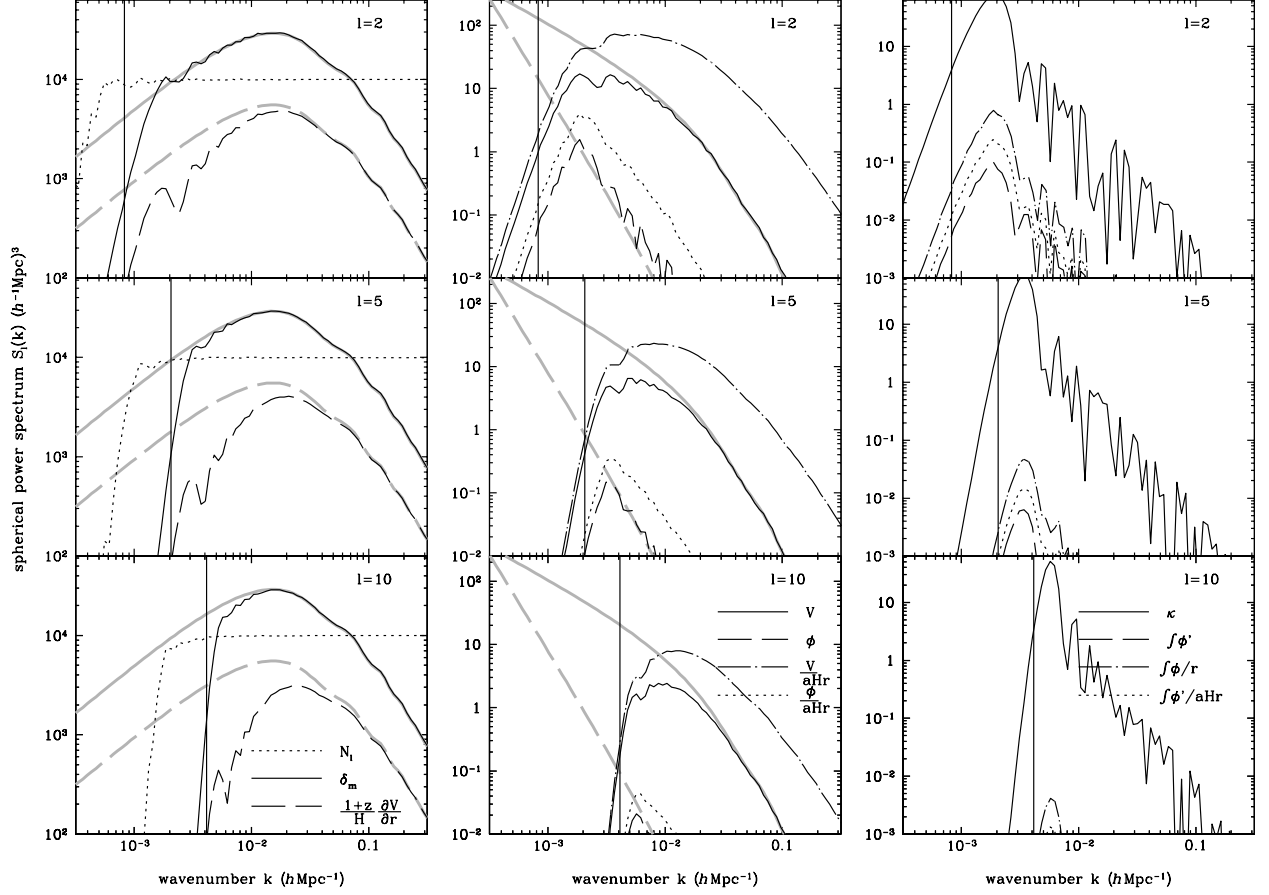


FIG. 3: Spherical power spectra with top-hat window function, in the same format as in Fig. 2. The general trend in the spherical power spectra are similar, but oscillations are imprinted in the spherical power spectra, due to the incomplete cancellation of the spherical Bessel function, imposed by the top-hat window function. The gray curves are identical to those in Fig. 2.

of the three-dimensional power spectra is somewhat extended to lower k than in Fig. 2.

A similar pattern is observed for the line-of-sight velocity $\mathcal{S}_l^V(k)$ and the potential $\mathcal{S}_l^\phi(k)$ spherical power spectra in the second column. Due to additional suppression factor $1/k^2$ in the weight function for the potential ϕ , more weight is given to large r at a given k for ϕ than for V , which results in oscillations in $\mathcal{S}_l^\phi(k)$ even at $k > 2\pi/(r_0/3)$. The remaining two curves (dot-dashed and dotted) in the radial distortion follow the same trend but, compared to Fig. 2, their peak is somewhat shifted to larger scale k due to the change in the window function.

The spherical power spectra of the projected quantities in the third column show the reversed trend, smooth power on large scales and oscillations on small scales, compared to the spherical power spectra in the first column. The projected quantities have additional integral in the spherical multipole function $\mathcal{M}_l(\vec{k}, k)$, and this line-of-sight integration cancels the oscillating part of the second spherical Bessel function, while the overall oscillation is determined by the first spherical Bessel function. The high- k oscillation arises

near $r \gg l/k$, at which there is no suppression in the top-hat window function. Furthermore, the peak position is shifted to smaller scales, since the mean distance to the source galaxies is smaller with the top-hat window function.

Having understood the key features in the spherical power spectra with the simplifying assumptions, we are now in a position to consider the full generality: time dependence of the transfer function and the weight function on the line-of-sight distance. In Fig. 4, we present the spherical power spectra with the Gaussian window function, explicitly accounting for their time dependence in the spherical multipole function. Overall, the spherical power spectra in Fig. 4 resemble those in Fig. 2, where the time dependence is neglected. The key difference in this case lies in the amplitude of the spherical power spectra, as the matter transfer function $\mathcal{T}_m(k, r)$ decreases in amplitude at $r > 0$ (i.e., $z > 0$).

The first column shows the spherical power spectra of the matter density (solid) and the redshift-space distortion (dashed). Compared to the flat-sky matter power spectrum (gray solid) at $z = 0$, the spherical power spectrum $\mathcal{S}_l^\delta(k)$ is lower in amplitude, as it is obtained by averaging over a

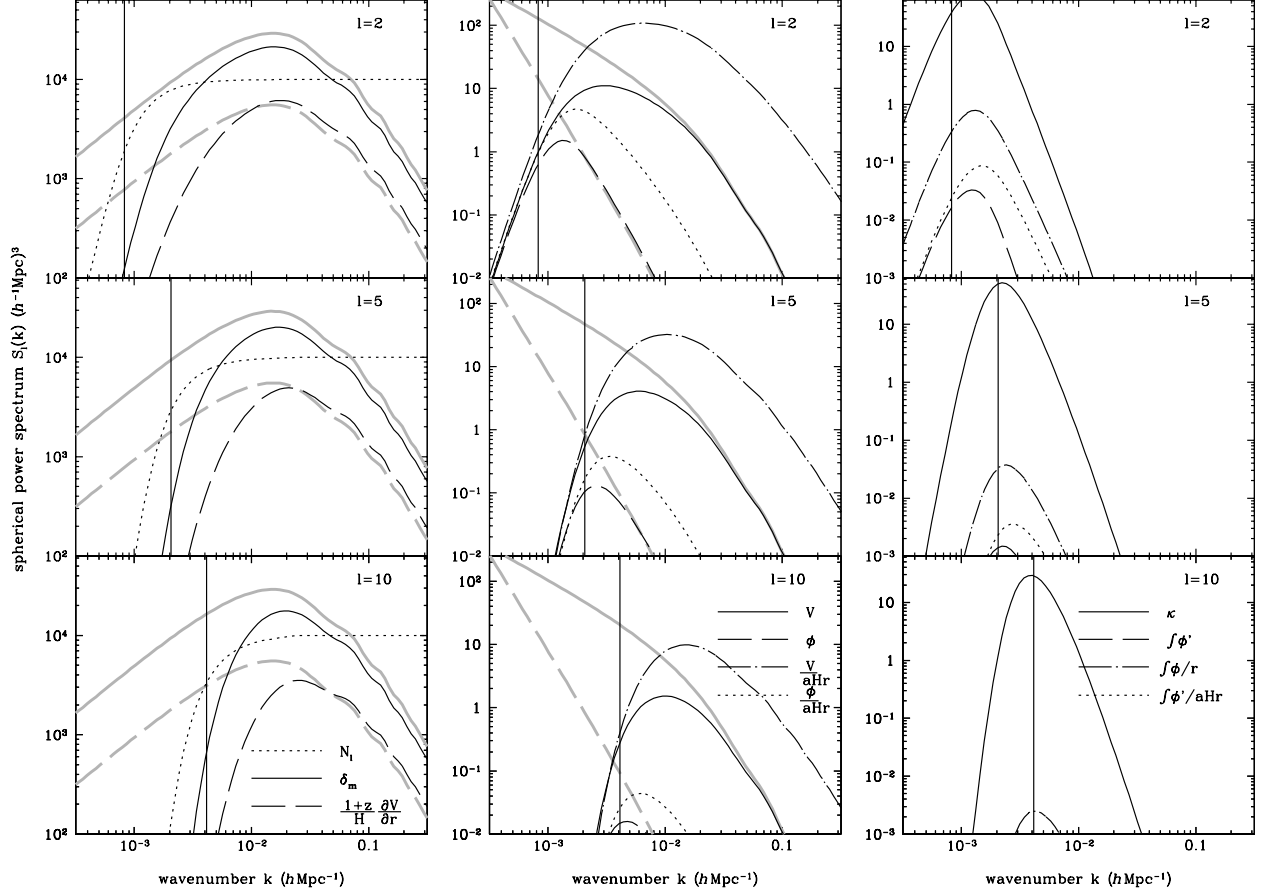


FIG. 4: Spherical power spectra with Gaussian window function. The time evolution of the transfer and the weight functions over the line-of-sight distance is explicitly computed. Compared to the spherical power spectra without evolution in Fig. 2, the spherical power spectra remain largely unaffected in shape, while the amplitude is naturally lower than the three-dimensional power spectra (gray) at $z = 0$. Various curves are in the same format as in Fig. 2.

range of redshift in Fig. 1. For the same reason, the logarithmic growth rate f is higher at $z > 0$, and hence the spherical power spectrum of the redshift-space distortion is higher in amplitude. The noise power spectrum (dotted) remains unchanged in Fig. 4, since the time dependence of the mean number density is already accounted by the survey window function in Fig. 2.

In the second column, the spherical power spectra of the line-of-sight velocity, the gravitational potential, and their variants show little difference, compared to those in Fig. 2. A small change in amplitude arises due to the shift in the peak line-of-sight distance. The velocity is nearly constant in redshift, while the gravitational potential is somewhat larger at $z > 0$, as dark energy domination leads to the decay in the gravitational potential. This trend is further reflected in the third column, where the projected quantities are displayed. The spherical power spectra of the gravitational lensing (solid) and the gravitational potential (dot-dashed) are slightly larger in amplitude, while the integrated Sachs-Wolfe contributions (dashed and dotted) are smaller, since the potential is constant

in the Einstein-de Sitter phase at $z > 0$.

B. Statistical uncertainties

The covariance matrix of the spherical power spectrum $S_l(k, k)$ generally involves the power spectrum, bispectrum and trispectrum of the spherical Fourier modes $\delta_{lm}(k)$. Non-Gaussianity induced by nonlinear gravitational clustering or, possibly, already present in the initial conditions can generate significant covariance through the bispectrum and trispectrum. For simplicity, however, we will henceforth ignore these contributions and assume that $\delta_{lm}(k)$ is simply Gaussian.

We begin with the calculation of the covariance of the spherical power spectrum assuming an all-sky experiment. At fixed multipole l , $S_l(k, k)$ can be estimated by averaging over all m and a thin wavenumber interval Δk and by subtracting the shot-noise component. However, since the shot-noise contribution \mathcal{N}_l is difficult to compute without precise knowledge of the radial selection function, we simply present the ob-

served spherical power spectrum, i.e., without shot-noise subtraction. We thus define an estimator of the spherical power spectrum

$$\hat{S}_l(k, k) = \frac{1}{2l+1} \sum_m \frac{1}{\Delta k} \int_{\Delta k} du |\delta_{lm}(u)|^2, \quad (76)$$

$$\text{Cov}[\hat{S}_l(k, k), \hat{S}_{l'}(k', k')] = \frac{1}{(2l+1)(2l'+1)} \sum_{m, m'} \frac{1}{(\Delta k)^2} \int_{\Delta k} du \int_{\Delta k} du' \left[\langle |\delta_{lm}(u)|^2 |\delta_{l'm'}(u')|^2 \rangle - \langle |\delta_{lm}(u)|^2 \rangle \langle |\delta_{l'm'}(u')|^2 \rangle \right]. \quad (77)$$

The assumption of Gaussian random fields considerably simplifies the evaluation of the trispectrum. A straightforward application of Wick's theorem yields

$$\begin{aligned} \text{Cov}[\hat{S}_l(k, k), \hat{S}_{l'}(k', k')] &= \frac{1}{(2l+1)^2} \sum_{m, m'} \frac{1}{(\Delta k)^2} \int_{\Delta k} du \int_{\Delta k} du' \left[\bar{S}_l(u, u') + \mathcal{N}_l(u, u') \right]^2 (\delta_{m, m'} + \delta_{m, -m'}) \delta_{ll'} \\ &= \frac{2}{2l+1} \frac{1}{(\Delta k)^2} \int_{\Delta k} du \int_{\Delta k} du' \left[\bar{S}_l(u, u') + \mathcal{N}_l(u, u') \right]^2 \delta_{ll'}. \end{aligned} \quad (78)$$

In the flat-sky approximation, estimates from different band-powers are uncorrelated in the Gaussian limit, so that the covariance of power spectrum estimators $\text{Cov}[\hat{P}(k_i), \hat{P}(k_j)]$ is proportional to $2P(k_i)P(k_j)\delta_{k_i, k_j}$. In the spherical Fourier decomposition, the Limber approximation shows that, for the matter (and potential) perturbations, band-power estimates of the spherical power spectrum are also uncorrelated. However, contributions from, e.g., the line-of-sight velocity or z-distortions will introduce covariance between measurements from different band-powers.

For shorthand convenience, let us now define

$$S_l(k) \equiv \bar{S}_l(k) + \mathcal{N}_l(k), \quad (79)$$

If we restrict ourselves to a galaxy sample of constant comoving density $\bar{n}_g = \tilde{n}_g = N_s/V_s$ and Poisson white noise, the error on $\hat{S}_l(k)$ scales as

$$[\Delta \hat{S}_l(k)]^2 = \frac{2}{2l+1} \left[\bar{S}_l(k) + \frac{1}{\bar{n}_g} \right]^2 \quad (80)$$

for infinitely narrow k bins ($\Delta k \rightarrow 0$). Equation (80) is the intrinsic error in $\hat{S}_l(k)$, reduced by the number of angular mode l available in the all-sky survey volume. This expression is a 2D analogy to the FKP expression [36] in 3D, except that the number $N(k)/2$ of independent modes in a k -shell is replaced by the number $(2l+1)/2$ of independent $|klm\rangle$ modes at fixed k and l . In general, however, the survey window function is not uniform and $1/\bar{n}_g$ must be replaced by the line-of-sight integral $\mathcal{N}_l(k)$. In addition to angular modes, there exist more radial modes available in the survey. The cumulative signal-to-noise for a measurement of \bar{S}_l is then

$$\left(\frac{S}{N} \right)^2 = \frac{V_s^{1/3}}{2} \sum_{l=2}^{l_{\max}} \left(\frac{2l+1}{2} \right) \int_{k_{\min}}^{k_{\max}} \frac{dk}{2\pi} \left(\frac{\bar{S}_l(k)}{\mathcal{N}_l(k) + \bar{S}_l(k)} \right)^2, \quad (81)$$

where the integration runs over the domain $[k - \Delta k/2, k + \Delta k/2]$, given a chosen band width Δk . The covariance of this (unbiased) band-power estimator is

where $V_s^{1/3}k$ is the number of radial modes at k . We introduced an extra multiplicative factor of $V_s^{1/3}$ (which is the only scale in the problem) in order to get a dimensionless quantity. This step can be made more rigorous by considering pixelized window functions along the line of sight. Going into this level of details is, however, beyond the scope of this work. The factor of $1/2$ arises from the fact that $\delta(\mathbf{x})$ is real, i.e. $\delta_{lm}^*(k) = \delta_{l-m}(k)$. Note that the cumulative signal-to-noise for a measurement of, e.g., the spherical power induced by the line-of-sight velocity is given by the same formula with S_l^V replacing \bar{S}_l in the numerator.

In order to establish a correspondence with mode counting in the 3D flat case, let us consider the limit $\bar{S}_l \gg \mathcal{N}_l$. Let also $L = V_s^{1/3}$ and ΔL be the characteristic length and resolution of the survey. The maximum wavenumber and wavenumber resolution thus are $k_{\max} = 2\pi/\Delta L$ and $\Delta k = 2\pi/L$. The angular resolution of the survey is $\theta \sim \Delta L/L$, which yields a maximum multipole $l_{\max} \sim 1/\theta \sim k_{\max}/\Delta k$. Therefore, the signal-to-noise is

$$\begin{aligned} \left(\frac{S}{N} \right)^2 &\simeq \frac{1}{4} l_{\max} (l_{\max} + 2) \left(\frac{k_{\max}}{\Delta k} \right) \\ &\simeq \frac{1}{4} \left(\frac{k_{\max}}{\Delta k} \right)^3. \end{aligned} \quad (82)$$

This is equal (up to a factor of order unity) to the signal-to-noise in the flat-sky limit,

$$\begin{aligned} \left(\frac{S}{N} \right)^2 &= \frac{V_s}{2} \times 2\pi \int \frac{dk_{\perp} k_{\perp}}{(2\pi)^2} \int \frac{dk_{\parallel}}{2\pi} \\ &\simeq \frac{\pi}{2} \left(\frac{k_{\max}^2 - k_{\min}^2}{\Delta k^2} \right) \left(\frac{k_{\max} - k_{\min}}{\Delta k} \right) \\ &\simeq \frac{\pi}{2} \left(\frac{k_{\max}}{\Delta k} \right)^3, \end{aligned} \quad (83)$$

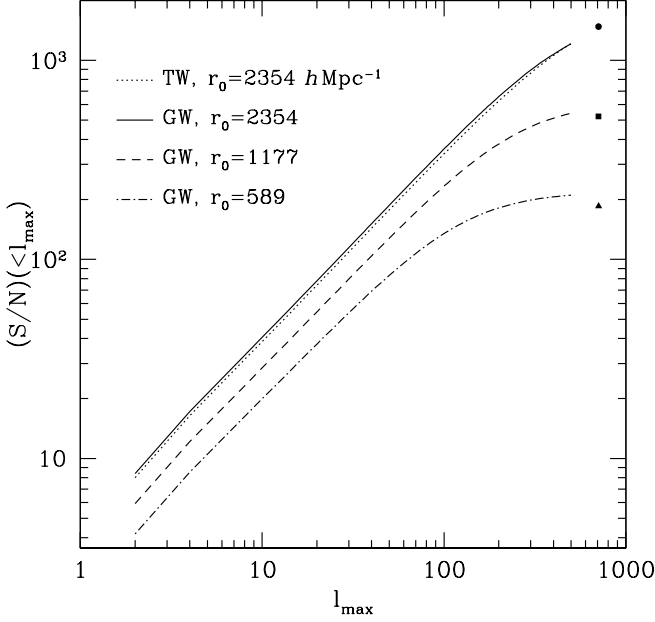


FIG. 5: Signal-to-noise for a measurement of the spherical power spectrum of galaxies with constant bias $b = 2$ (see text). Results are shown as a function of the maximum multipole l_{\max} . The curves show Eq. (85) for the tophat (TW) and Gaussian (GW) survey window with several choices of r_0 . The filled symbols show S/N in the flat-sky approximation (Eq. [85]) for the Gaussian survey window with $r_0 = 2354$ (circle), 1177 (square) and $589 h^{-1} \text{Mpc}$ (triangle). Note that their abscisse is arbitrary.

where the last equality assumes $k_{\min} \ll k_{\max}$. When dealing with real galaxy data however, one must take into account the shot-noise and the survey window function. Ignoring contributions others than fluctuations in the matter density, the Limber approximation gives

$$\left(\frac{S}{N}\right)_{l < l_{\max}}^2 \approx \frac{V_s^{1/3}}{2} \sum_{l=2}^{l_{\max}} \left(\frac{2l+1}{2}\right) \times \int_0^\infty \frac{dk}{2\pi} \left(\frac{\tilde{n}_g \mathcal{W}(\frac{\nu}{k}) P_m(k, \frac{\nu}{k})}{1 + \tilde{n}_g \mathcal{W}(\frac{\nu}{k}) P_m(k, \frac{\nu}{k})}\right)^2. \quad (84)$$

In Fig. 5, this expression is evaluated as a function of l_{\max} for the Gaussian (GW) and tophat (TW) survey window considered in Sec. §IV (dotted and solid curves). The galaxy bias is assumed to be constant, $b = 2$, and the z -dependence of the matter power spectrum has been neglected, i.e., $P_m(k, r) = P_m(k, 0)$. To exemplify the scaling $(S/N) \propto V_s^{1/6}$, results are also shown for the Gaussian window with 1/8 and 1/64 the fiducial volume $V_s \approx 55 h^{-1} \text{Gpc}$. The signal-to-noise eventually saturates at large values of l_{\max} because, for $l \gg 1$, the Gaussian window $\mathcal{W}(\nu/k) \sim \exp[-(l/kr_0)^2]$ only picks up (small-scale) measurements that are shot-noise dominated. For our choice of b , this occurs at $k \sim 0.2 h^{-1} \text{Mpc}$. As a result, the signal-to-noise flattens out around $l_{\max} \sim kr_0 \sim 400$ ($r_0 = 2354 h^{-1} \text{Mpc}$) and ~ 100 ($r_0 = 589 h^{-1} \text{Mpc}$). The filled symbols represent the signal-to-noise in the flat-sky ap-

proximation,

$$\left(\frac{S}{N}\right)^2 = \frac{1}{\pi} \int_0^\infty dr r^2 \int_0^\infty dk k^2 \left(\frac{\tilde{n}_g \mathcal{W}(r) P_m(k, r)}{1 + \tilde{n}_g \mathcal{W}(r) P_m(k, r)}\right)^2, \quad (85)$$

computed for the Gaussian survey window with $r_0 = 2354$ (circle), 1177 (square) and $589 h^{-1} \text{Mpc}$ (triangle). The flat-sky estimates are consistent with the Limber-approximated $(S/N)(< l_{\max})$ in the limit $l_{\max} \gg 1$. This provides support for the validity of Eq. (85).

V. DISCUSSION

We have performed an all-sky analysis of the galaxy power spectrum, accounting for all the relativistic effects in galaxy clustering. The spherical Fourier analysis has been well developed in galaxy clustering [25–27], while its application to galaxy clustering has been limited to the Kaiser formula [52]. We have used the spherical Fourier analysis to analyze the full relativistic formula. The observed galaxy fluctuation is decomposed in terms of spherical harmonics and spherical Bessel functions that are angular and radial eigenfunctions of the Helmholtz equation, providing a natural basis for the observer at origin to describe the galaxy clustering measurements on the observed sphere.

In light of the recent development in the relativistic formulation of galaxy clustering [9, 10], there exist numerous relativistic effects in galaxy clustering, in addition to the standard redshift-space distortion effect. These relativistic effects become substantial on very large scales, and measurements of these large-scale modes inevitably invoke complications associated with the flat-sky approximation and the survey geometries. By using the spherical harmonics for its angular decomposition, the spherical power spectrum is independent of the validity of the flat-sky approximation, while it retains the advantage of the standard Fourier analysis, namely, the simple and physically intuitive interpretation of the measurements in conjunction with the underlying matter distribution.

We have computed the spherical Fourier power spectrum of the observed galaxy distribution, accounting for the relativistic effects. Compared to the standard Newtonian description, there exist additional contributions to the observed galaxy fluctuation, and these additional contributions can be categorized as the matter density fluctuation, the line-of-sight velocity contribution, the gravitational potential contribution, and the line-of-sight projection contribution [12–16]. The spherical power spectrum of the matter density is identical to the usual three-dimensional matter power spectrum $S_l^\delta(k) \simeq P_m(k)$, regardless of its angular multipole l , as the matter power spectrum is isotropic. This correspondence greatly facilitates the physical interpretation of the measurements.

Since the line-of-sight velocity affects the observed distance to the galaxies in redshift space, the velocity contribution in galaxy clustering is angular dependent. Therefore, the spherical power spectrum $S_l^V(k)$ of the velocity contribution is similar to its three-dimensional counterpart $P_V(k, \mu_k)$, but its angular dependence is encoded as a function of angu-

lar multipole l : At a given amplitude k of a wavevector \mathbf{k} , higher angular multipoles represent larger transverse modes, or lower cosine angle $\mu_k = k_{\parallel}/k$. The redshift-space distortion effect arises from the spatial derivative of the line-of-sight velocity, and its spherical power spectrum $\mathcal{S}_l^z(k)$ follows the similar trend, as its three-dimensional power spectrum is $P_z(k, \mu_k) = f^2 \mu_k^4 P_m(k)$.

The gravitational potential contribution to the observed galaxy fluctuation can be readily computed from the spherical Fourier decomposition. Similar to the case of the matter density fluctuation, the gravitational potential power spectrum $P_\phi(k)$ is isotropic, and the spherical power spectrum for the gravitational potential is identical to the three-dimensional power spectrum $\mathcal{S}_l^\phi(k) \simeq P_\phi(k)$, regardless of its angular multipole. Furthermore, while the gravitational potential contribution to the variance of galaxy clustering often diverges due to its scale-free nature, the spherical power spectrum is unaffected by this problem since it measures individual modes of fluctuations as in the traditional power spectrum analysis.

The other contributions to the observed galaxy fluctuation, such as the gravitational lensing and the integrated Sachs-Wolfe effects, arise from fluctuations along the line-of-sight direction. Since these projected quantities are intrinsically angular, it is difficult to handle their contribution in the standard power spectrum analysis. However, with its angular decomposition using spherical harmonics, the spherical Fourier analysis can naturally implement the contribution of the projected quantities to galaxy clustering. With the sole exception of the gravitational lensing effect, we find that compared to the matter density fluctuation, the contribution of the projected quantities are negligible, and this justifies the simplification of ignoring the projected quantities in the power spectrum analysis [10, 17]. Moreover, the spherical power spectrum $\mathcal{S}_l^c(k)$ of the gravitational lensing contribution in galaxy clustering is also known as 3D weak lensing [32, 33], where the information on radial distances to the background source galaxies is

utilized to map the matter distribution in 3D, as opposed to the traditional 2D weak lensing. Our spherical Fourier analysis provides a complete and comprehensive description of galaxy clustering and its associated effects.

We have derived the covariance matrix of the spherical power spectrum, assuming that the matter density fluctuation is the dominant contribution. The covariance matrix of the spherical power spectrum asymptotically matches that of the three-dimensional power spectrum on small scales. It is also shown [10, 17, 24] that since the volume available for galaxy surveys at low redshift is relatively small, there are too few large-scale modes that are sensitive to the relativistic effect in galaxy clustering. Therefore, it makes little difference in terms of measurement significance, if one chooses to embed the observed sphere in a cubic volume and performs the standard Fourier analysis, instead of performing the spherical Fourier analysis. However, the spherical Fourier analysis presented in this paper provides a more natural way to analyze the full relativistic effects in galaxy clustering. Furthermore, it is shown [17] that the multi-tracer analysis [53] with the shot-noise cancelling technique [54] can substantially enhance the measurement significance of the relativistic effects in galaxy clustering, in which case we expect that the spherical Fourier analysis becomes essential in describing the measurements on large scales.

Acknowledgments

We acknowledge useful discussions with Ruth Durrer, Ue-Li Pen, Uroš Seljak, Zvonimir Vlah. J.Y. is supported by the SNF Ambizione Grant. V.D. acknowledges support from the Swiss National Science Foundation and is grateful for the hospitality of the Aspen Center for Physics, where part of this work was completed.

-
- [1] D. G. York et al., *Astron. J.* **120**, 1579 (2000), arXiv:astro-ph/0006396.
 - [2] M. Colless et al., *Mon. Not. R. Astron. Soc.* **328**, 1039 (2001), arXiv:astro-ph/0106498.
 - [3] D. J. Schlegel, M. Blanton, D. Eisenstein, et al., in *American Astronomical Society Meeting Abstracts* (2007), vol. 211 of *IOP Philadelphia, PA, 2007*, pp. 132.29–+.
 - [4] The Dark Energy Survey Collaboration (2005), arXiv:astro-ph/0510346.
 - [5] M. J. Drinkwater, R. J. Jurek, C. Blake, D. Woods, et al., *Mon. Not. R. Astron. Soc.* **401**, 1429 (2010), 0911.4246.
 - [6] M. Tegmark et al., *Astrophys. J.* **606**, 702 (2004), arXiv:0310725.
 - [7] W. J. Percival, R. C. Nichol, D. J. Eisenstein, D. H. Weinberg, M. Fukugita, A. C. Pope, D. P. Schneider, A. S. Szalay, M. S. Vogeley, I. Zehavi, et al., *Astrophys. J.* **657**, 51 (2007), arXiv:astro-ph/0608635.
 - [8] B. A. Reid, W. J. Percival, D. J. Eisenstein, L. Verde, D. N. Spergel, R. A. Skibba, N. A. Bahcall, et al., *Mon. Not. R. Astron. Soc.* **404**, 60 (2010), 0907.1659.
 - [9] J. Yoo, A. L. Fitzpatrick, and M. Zaldarriaga, *Phys. Rev. D* **80**, 083514 (2009), arXiv:0907.0707.
 - [10] J. Yoo, *Phys. Rev. D* **82**, 083508 (2010), arXiv:1009.3021.
 - [11] J. Yoo, *Phys. Rev. D* **79**, 023517 (2009), arXiv:0808.3138.
 - [12] A. Challinor and A. Lewis, *Phys. Rev. D* **84**, 043516 (2011), arXiv:1105.5292.
 - [13] C. Bonvin and R. Durrer, *Phys. Rev. D* **84**, 063505 (2011), arXiv:1105.5280.
 - [14] T. Baldauf, U. Seljak, L. Senatore, and M. Zaldarriaga, *J. Cosmol. Astropart. Phys.* **10**, 31 (2011), arXiv:1106.5507.
 - [15] M. Bruni, R. Crittenden, K. Koyama, R. Maartens, C. Pitrou, and D. Wands, *Phys. Rev. D* **85**, 041301 (2012), arXiv:1106.3999.
 - [16] D. Jeong, F. Schmidt, and C. M. Hirata, *Phys. Rev. D* **85**, 023504 (2012), arXiv:1107.5427.
 - [17] J. Yoo, N. Hamaus, U. Seljak, and M. Zaldarriaga, *Phys. Rev. D* **86**, 063514 (2012), 1206.5809.
 - [18] A. S. Szalay, T. Matsubara, and S. D. Landy, *Astrophys. J. Lett.* **498**, L1 (1998), arXiv:9712007.
 - [19] I. Szapudi, *Astrophys. J.* **614**, 51 (2004), arXiv:0404477.

[20] T. Matsubara, *Astrophys. J.* **535**, 1 (2000), arXiv:9908056.
 [21] P. Pápai and I. Szapudi, *Mon. Not. R. Astron. Soc.* **389**, 292 (2008), arXiv:0802.2940.
 [22] F. Montanari and R. Durrer, *Phys. Rev. D* **86**, 063503 (2012), 1206.3545.
 [23] D. Bertacca, R. Maartens, A. Raccaelli, and C. Clarkson, *J. Cosmol. Astropart. Phys.* **10**, 25 (2012), 1205.5221.
 [24] J. Yoo and U. Seljak, *Mon. Not. R. Astron. Soc.* (2013), in preparation.
 [25] J. Binney and T. Quinn, *Mon. Not. R. Astron. Soc.* **249**, 678 (1991).
 [26] K. B. Fisher, O. Lahav, Y. Hoffman, D. Lynden-Bell, and S. Zaroubi, *Mon. Not. R. Astron. Soc.* **272**, 885 (1995), arXiv:9406009.
 [27] A. F. Heavens and A. N. Taylor, *Mon. Not. R. Astron. Soc.* **275**, 483 (1995), arXiv:9409027.
 [28] K. B. Fisher, C. A. Scharf, and O. Lahav, *Mon. Not. R. Astron. Soc.* **266**, 219 (1994), arXiv:9309027.
 [29] A. Rassat and A. Refregier, *Astron. Astrophys.* **540**, A115 (2012), 1112.3100.
 [30] G. Pratten and D. Munshi, *ArXiv e-prints* (2013), 1301.3673.
 [31] C. Shapiro, R. G. Crittenden, and W. J. Percival, *Mon. Not. R. Astron. Soc.* **422**, 2341 (2012), 1109.1981.
 [32] A. Heavens, *Mon. Not. R. Astron. Soc.* **343**, 1327 (2003), arXiv:0304151.
 [33] T. D. Kitching, A. F. Heavens, and L. Miller, *Mon. Not. R. Astron. Soc.* **413**, 2923 (2011), arXiv:1007.2953.
 [34] E. Komatsu, K. M. Smith, J. Dunkley, C. L. Bennett, B. Gold, G. Hinshaw, N. Jarosik, D. Larson, M. R. Nolte, L. Page, et al., *Astrophys. J. Suppl. Ser.* **192**, 18 (2011), 1001.4538.
 [35] A. J. S. Hamilton and M. Culhane, *Mon. Not. R. Astron. Soc.* **278**, 73 (1996), arXiv:9507021.
 [36] H. A. Feldman, N. Kaiser, and J. A. Peacock, *Astrophys. J.* **426**, 23 (1994), arXiv:astro-ph/9304022.
 [37] J. M. Bardeen, *Phys. Rev. D* **22**, 1882 (1980).
 [38] H. Kodama and M. Sasaki, *Progress of Theoretical Physics Supplement* **78**, 1 (1984).
 [39] J.-C. Hwang and H. Noh, *Phys. Rev. D* **65**, 023512 (2001), arXiv:0102005.
 [40] J. Hwang and H. Noh, *Gen. Relativ. Gravit.* **31**, 1131 (1999), arXiv:9907063.
 [41] J.-C. Hwang and H. Noh, *Phys. Rev. D* **72**, 044011 (2005), arXiv:0412128.
 [42] L. Lopez-Honorez, O. Mena, and S. Rigolin, *Phys. Rev. D* **85**, 023511 (2012), 1109.5117.
 [43] A. Hall, C. Bonvin, and A. Challinor, *ArXiv e-prints* (2012), 1212.0728.
 [44] L. Lombriser, J. Yoo, and K. Koyama, *ArXiv e-prints* (2013), 1301.3132.
 [45] D. N. Limber, *Astrophys. J.* **117**, 134 (1953).
 [46] N. Kaiser, *Astrophys. J.* **388**, 272 (1992).
 [47] M. LoVerde and N. Afshordi, *ArXiv e-prints* (2008), 0809.5112.
 [48] F. Bernardeau, C. Bonvin, N. Van de Rijdt, and F. Vernizzi, *ArXiv e-prints* (2011), 1112.4430.
 [49] I. S. Gradshteyn and I. M. Ryzhik, *Table of Integrals, Series, and Products* (2007).
 [50] L. Hui, E. Gaztañaga, and M. Loverde, *Phys. Rev. D* **77**, 063526 (2008), arXiv:0710.4191.
 [51] P. G. Castro, A. F. Heavens, and T. D. Kitching, *Phys. Rev. D* **72**, 023516 (2005), arXiv:0503479.
 [52] N. Kaiser, *Mon. Not. R. Astron. Soc.* **227**, 1 (1987).
 [53] U. Seljak, *Phys. Rev. Lett.* **102**, 021302 (2009), 0807.1770.

[54] U. Seljak, N. Hamaus, and V. Desjacques, *Phys. Rev. Lett.* **103**, 091303 (2009), 0904.2963.

Appendix A: Top-hat normalization

Here we derive the normalization coefficient for the top-hat window function in Eq. (74). The normalization coefficient can be obtained by computing the spherical power spectrum for the matter density

$$S_l^\delta(k, k) = \int d\tilde{k} P_m(\tilde{k}) \left[\frac{2 k \tilde{k}}{\pi} \int_0^{r_0} dr r^2 j_l(kr) j_l(\tilde{k}r) \right]^2, \quad (\text{A1})$$

and taking the limit ($k \rightarrow \infty$). We first define the integrand

$$F(k, \tilde{k}) \equiv \frac{2 k \tilde{k}}{\pi} \int_0^{r_0} dr r^2 j_l(kr) j_l(\tilde{k}r), \quad (\text{A2})$$

and then arrange Eq. (A1) as

$$S_l^\delta(k, k) = \int_{-\infty}^{\infty} d\bar{k} P_m(k + \bar{k}) [F(k, k + \bar{k})]^2. \quad (\text{A3})$$

Since the integrand peaks around $k \simeq \bar{k}$, we take the limit ($k \rightarrow \infty$) and expand the integrand $F(k, k + \bar{k})$:

$$\begin{aligned} \lim_{k \rightarrow \infty} S_l^\delta(k, k) &\simeq P_m(k) \int_{-\infty}^{\infty} d\bar{k} \left[\mathcal{F} + \frac{\bar{k}^2}{2} \mathcal{F}'' + \dots \right]^2 \\ &= P_m(k) \sqrt{2\pi} \mathcal{F}^2 \left[-\frac{\mathcal{F}}{2\mathcal{F}''} \right]^{1/2}, \end{aligned} \quad (\text{A4})$$

where we performed a Gaussian integral. The asymptotic values of the integrand are

$$\mathcal{F} \equiv \lim_{k \rightarrow \infty} F(k) = \lim_{k \rightarrow \infty} \frac{2r_0}{\pi x} \int_0^x dx x^2 j_l^2(x) = \frac{r_0}{\pi}, \quad (\text{A5})$$

$$\begin{aligned} \mathcal{F}'' &\equiv \lim_{k \rightarrow \infty} F''(k) = \lim_{k \rightarrow \infty} \frac{2r_0^3}{\pi x^3} \int_0^x dx x^4 j_l(x) \left[\frac{2}{x} j_l'(x) + j_l''(x) \right] \\ &= -\frac{r_0^3}{3\pi}, \end{aligned} \quad (\text{A6})$$

and we obtain the normalization coefficient in Eq. (74)

$$\lim_{k \rightarrow \infty} S_l^\delta(k, k) = P_m(k) \frac{r_0}{\pi} \sqrt{\frac{3}{\pi}}. \quad (\text{A7})$$

Appendix B: Covariance of the spherical power spectrum

Here we present details of the calculation of the covariance matrix of the spherical power spectrum estimator. We will omit the band-power averaging for the sake of conciseness. Using Eq. (16), the four-point correlator of the spherical Fourier modes reads

$$\begin{aligned} \langle \delta_{lm}(k) \delta_{lm}^*(k) \delta_{l'm'}(k') \delta_{l'm'}^*(k') \rangle &= \left(\frac{2}{\pi} \right)^2 k^2 k'^2 \prod_{i=1}^4 \left\{ \int d^3 x_i \right\} j_l(kr_1) j_l(kr_2) j_l(k'r_3) j_l(k'r_4) \\ &\times Y_{lm}^*(\hat{\mathbf{x}}_1) Y_{lm}(\hat{\mathbf{x}}_2) Y_{l'm'}^*(\hat{\mathbf{x}}_3) Y_{l'm'}(\hat{\mathbf{x}}_4) \langle \delta(\mathbf{x}_1) \delta(\mathbf{x}_2) \delta(\mathbf{x}_3) \delta(\mathbf{x}_4) \rangle. \end{aligned} \quad (\text{B1})$$

Assuming the galaxy overdensity field $\delta(\mathbf{x})$ follows Gaussian statistics, the four-point correlator in the right-hand side reduces to the sum of three products of two-point correlation functions, whose explicit expression is given by Eq. (23) divided by \tilde{n}_g^2 . The contribution that involves $\langle \delta_g(\mathbf{x}_1) \delta_g(\mathbf{x}_2) \rangle \langle \delta_g(\mathbf{x}_3) \delta_g(\mathbf{x}_4) \rangle$ exactly cancels out the term $\langle |\delta_{lm}(k)|^2 \rangle \langle |\delta_{l'm'}(k')|^2 \rangle$ in the covariance matrix in Eq. (77). To compute the two other contributions, we must evaluate, e.g.,

$$\begin{aligned} J_{14} &\equiv \frac{2}{\pi} k k' \int dr_1 r_1^2 \int dr_4 r_4^2 j_l(kr_1) j_{l'}(k'r_4) \int d^2 \hat{\mathbf{x}}_1 \int d^2 \hat{\mathbf{x}}_4 Y_{lm}^*(\hat{\mathbf{x}}_1) Y_{l'm'}(\hat{\mathbf{x}}_4) \\ &\times \left\{ \mathcal{W}(r_1) \mathcal{W}(r_4) [1 + \xi_g(\mathbf{x}_1 - \mathbf{x}_4)] + \frac{1}{\tilde{n}_g} \mathcal{W}(r_1) \delta^D(\mathbf{x}_1 - \mathbf{x}_4) \right\}. \end{aligned} \quad (\text{B2})$$

On expressing $\xi_g(\mathbf{x}_1 - \mathbf{x}_4)$ as the Fourier transform

$$\xi_g(\mathbf{x}_1 - \mathbf{x}_4) = \int \frac{d^3 k}{(2\pi)^3} \mathcal{T}_g(k, r_1) \mathcal{T}_g(k, r_4) P_{\varphi_v}(k) e^{i\mathbf{k} \cdot (\mathbf{x}_1 - \mathbf{x}_4)}, \quad (\text{B3})$$

and inserting the Rayleigh expansion in Eq. (9), the integrals over the angular variables simplify to

$$\int d^2 \hat{\mathbf{x}}_1 \int d^2 \hat{\mathbf{x}}_4 Y_{lm}^*(\hat{\mathbf{x}}_1) Y_{l'm'}(\hat{\mathbf{x}}_4) e^{i\mathbf{k} \cdot (\mathbf{x}_1 - \mathbf{x}_4)} = (4\pi)^2 i^{l-l'} j_l(kr_1) j_{l'}(kr_4) Y_{lm}^*(\hat{\mathbf{k}}) Y_{l'm'}(\hat{\mathbf{k}}). \quad (\text{B4})$$

As a consequence, the contribution of $\xi_g(\mathbf{x}_1 - \mathbf{x}_4)$ to J_{14} becomes

$$\begin{aligned} &32\pi k k' i^{l-l'} \int dr_1 r_1^2 \int dr_4 r_4^2 \mathcal{W}(r_1) \mathcal{W}(r_4) j_l(kr_1) j_{l'}(k'r_4) \int \frac{d^3 \tilde{k}}{(2\pi)^3} \mathcal{T}_g(\tilde{k}, r_1) \mathcal{T}_g(\tilde{k}, r_4) j_l(\tilde{k}r_1) j_{l'}(\tilde{k}r_4) Y_{lm}^*(\hat{\mathbf{k}}) Y_{l'm'}(\hat{\mathbf{k}}) P_{\varphi_v}(\tilde{k}) \\ &= (4\pi) \int d \ln \tilde{k} \Delta_{\varphi_v}^2(\tilde{k}) \left[\frac{2}{\pi} k k' \int dr_1 r_1^2 \mathcal{W}(r_1) j_l(kr_1) j_{l'}(\tilde{k}r_1) \mathcal{T}_g(\tilde{k}, r_1) \times \int dr_4 r_4^2 \mathcal{W}(r_4) j_l(kr_4) j_{l'}(\tilde{k}r_4) \mathcal{T}_g(\tilde{k}, r_4) \right] \delta_{ll'} \delta_{mm'} \\ &= \mathcal{S}_l(k, k') \delta_{ll'} \delta_{mm'}. \end{aligned} \quad (\text{B5})$$

Similarly, using $\delta^D(\mathbf{x}_1 - \mathbf{x}_4) = \delta^D(r_1 - r_4) \delta^D(\hat{\mathbf{x}}_1 - \hat{\mathbf{x}}_4)/r_1^2$ and the orthonormality of the spherical harmonics, the contribution of the Poisson noise term to J_{14} is

$$\frac{2kk'}{\pi \tilde{n}_g} \int dr_1 r_1^2 \int dr_4 r_4^2 \mathcal{W}(r_1) j_l(kr_1) j_{l'}(k'r_4) \delta^D(r_1 - r_4) \int d^2 \hat{\mathbf{x}}_1 Y_{lm}^*(\hat{\mathbf{x}}_1) Y_{l'm'}(\hat{\mathbf{x}}_1) = \mathcal{N}_l(k, k') \delta_{ll'} \delta_{mm'}. \quad (\text{B6})$$

J_{14} is the sum of these two contributions, i.e. $J_{14} = [\mathcal{S}_l(k, k') + \mathcal{N}_l(k, k')] \delta_{ll'} \delta_{mm'}$. Symmetry considerations show that this holds true for J_{ij} , $i \neq j$. This leads to the desired result in Eq. (78).
